© Copyright 2024

Aaron Abeyta

An Experimental Approach for Characterizing Gas Flow in the Build Chamber of Laser Powder Bed Fusion Systems Utilizing Particle Image Velocimetry

Aaron Abeyta

A thesis submitted in partial fulfillment of the requirements for the degree of:

Master of Science

University of Washington

2024

Committee:

Dwayne Arola

Mamidala Ramulu

Owen Williams

Program Authorized to Offer Degree:

Materials Science and Engineering

University of Washington

Abstract

An Experimental Approach for Characterizing Gas Flow in the Build Chamber of Laser Powder Bed Fusion Systems Utilizing Particle Image Velocimetry

Aaron Abeyta

Chair of the Supervisory Committee:
Dwayne Arola
Materials Science & Engineering

Laser Powder Bed Fusion (LPBF) is a method of additive manufacturing (AM) for metals that is increasingly being utilized in the aerospace industry. In addition to its comparative low buy to fly ratio, LPBF enables the design and manufacture of components that were previously not possible with subtractive manufacturing techniques. Due to the high temperatures achieved in laser melting of the powder, an inert shielding gas is used to protect the melt pool from contamination by oxygen, hydrogen and other potential reactive elements in the build chamber. The inert gas (commonly Argon) is introduced with nozzles to achieve a cross-flow over the build surface that whisks away byproducts generated by the laser-powder interaction. However, spatial variations or other undesirable characteristics (e.g., turbulence, dead zones, etc.) in the gas flow distribution could cause defects in the metal, spatial variability in quality and microstructure, as well as mechanical property variability. That “intra-build” variability can limit

the application of LPBF and/or the application of parts produced by this technology for stress-critical applications.

This investigation analyzed the inert gas flow in a full-scale model of the EOS M290 build chamber utilizing high-fidelity Particle Image Velocimetry (PIV) in planar mode using air as the gas medium. Results showed that the gas flow within the build chamber of the EOS M290 is not uniform across the build plate. Based on planar mode views parallel to the build plate, there is a reduction in the velocity from the left to the right side of approximately 47%. In addition, there is a gradient in the flow from the gas inlet to the exit baffle of approximately 66%. Although the highest cross-flow velocity is near the left side of the build plate, there is a dead zone in the back left corner with no tangential cross-flow. A recirculation zone was observed immediately downstream of the inlet vent, that spanned the build plate width, indicating that the gas cross-flow did not envelop the entire build plate. A recirculation region was also identified in planes perpendicular to the build plate that develops approximately midway between the upper and lower inlet nozzles. Vortices in the flow within that region could entrain smoke and metal vapor condensate, which in turn could cause attenuation of the incident laser. The flow showed spatial variations in turbulent kinetic energy, which could serve as a useful parameter to assess particle entrainment. These results provide new understanding that supports the design of components by LPBF with improved quality, and that could aid in the development of new nozzle geometry designs for the EOS M290 to optimize the gas flow

Table of Contents

Table of Figures

ACKNOWLEDGEMENTS

I would first like to thank my friends, family, and my girlfriend for always supporting me and encouraging me to challenge myself. I would like to thank my PI and committee chair Prof. Dwayne Arola, for his guidance and support that made this thesis possible. An equal amount of thanks is necessary for the following individuals from The Boeing Company for their invaluable feedback and assistance that made this project possible: Troy Haworth, Ashley Jones, Julian Williams, and Eric Dalton. A very special thanks to Prof. Owen Williams for giving me access to the PIV equipment he is responsible for and for his helpful guidance on PIV theory and applications, and Prof. Mamidala Ramulu for his feedback and time. Thank you to the following undergraduates who worked with me as part of their senior capstone: Aaron Maschhoff, Jack Hardy, Marco Iacoviello, and Yuliya Pruzhanskaya. Finally, I would like to thank my colleagues in the Arola group for either lending a helping hand, sharing lab spaces, or giving me valuable feedback on my data presentations.

Chapter 1 INTRODUCTION

1.1 Laser Powder Bed Fusion

Laser Powder Bed Fusion (LPBF) is an additive manufacturing (AM) technology that has experienced considerable growth in applications within the aerospace industry for the manufacture of metal components. This process is capable of manufacturing novel components with designs that were previously not feasible using traditional methods of manufacturing for engineering materials, which consists of both addition and subtraction processes.

There are many apparent advantages to LPBF for aerospace, including the opportunity to design and manufacture components with unlimited complexity, as well as the ability to combine multiple parts of complicated systems into a single part. Another advantage is the unlimited customization, implying that a series of parts can be produced, each with adjustments of interest and that are being considered for new part prototypes. And perhaps the largest advantage in this industry is the potential for substantial reduction in both the purchase of materials that are required for the manufacturing process and that are used to support the component design, which is generally regarded as “minimum buy to fly”.

1.2 Build Process

The manufacture of components by LPBF proceeds by the selective melting of metal powder by a high-power laser in a layer-by-layer routine, as shown schematically in Figure 1.1. At the start of each layer of the build, a uniform layer of powder is distributed by a recoater blade or “rake” from the powder hopper. The laser then scans selected areas of the powder bed to melt and resolidify into a single layer of the part. After the laser scan is complete, the build plate is lowered, and a new layer is deposited. This iterative process repeats until the part is completed.

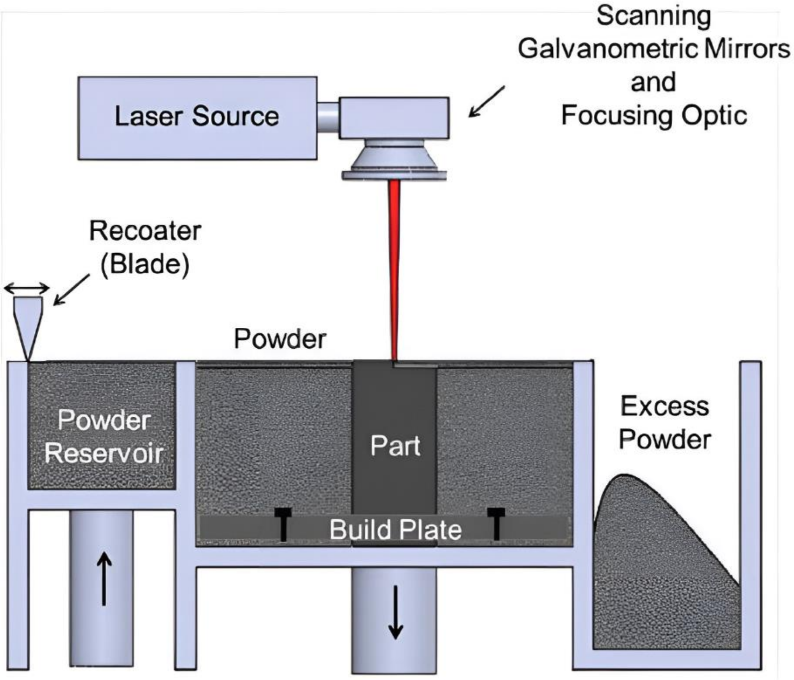

Figure 1.1 Schematic of the Laser Powder Bed Fusion Process [1].

Despite the many advantages of LPBF for the manufacture of components in the aerospace and medical industries, this technology has several limitations. Some of these impede its adoption for the manufacturing of stress critical and safety critical component parts, such as the interaction between the laser and metal powder during the melt process. As a result of the intense localized energy of the focused laser, as well as the melting of powder under the intense heat, a portion of the metal is vaporized and then condenses within a plume of smoke above the melt pool, as illustrated in Figure 1.2. This smoke can attenuate the incident laser power, thus reducing the effective intensity of the laser on the print bed and reducing the size and depth of the melt pool, which potentially results in poor fusion of the existing and preceding layers. In addition, spatter is often generated during the laser-powder interaction by multiple avenues as explained by Young et. al [2]. The first variant of spatter is solid and unmelted powder that is ejected by the laser prior to being sufficiently melted. Spatter can also be generated as liquid droplets, which are a byproduct of the metallic vapor generated during the melting process. The recoil pressure from the laser-melt pool interactions causes ejection of these liquid droplets, scattering them in areas outside of the melt pool. Powder and spatter can also agglomerate to form larger spatter particles. In addition, spatter can be induced by defects and contamination of the powder that are further discussed later in this thesis, which can cause instabilities in laser interaction with the powder and meltpool under specific process conditions. Sources of contamination may come from the powder composition or the atmosphere in the build chamber. To overcome the detrimental impact of these byproducts in LPBF, an inert gas is introduced within the build chamber and has become recognized as a critical requirement for the development of high-quality metal [3].

1.3 Inert Gas Flow

To minimize degradation of the molten metal caused by the arc atmosphere, LPBF systems utilize a constant cross-flow of an inert gas. The inert gas serves to prevent oxidation of metal within the melt pool and the surrounding powder that reaches elevated temperatures during the build process. Titanium and aluminum alloys have an affinity to react with oxygen in an ambient environment, especially at elevated temperatures, such as during the melt process. The inert gas flow also serves to whisk away the smoke and condensate described earlier, to prevent their associated defects from metabolizing. In general, argon appears to be the most commonly employed inert gas that is used in LPBF [4].

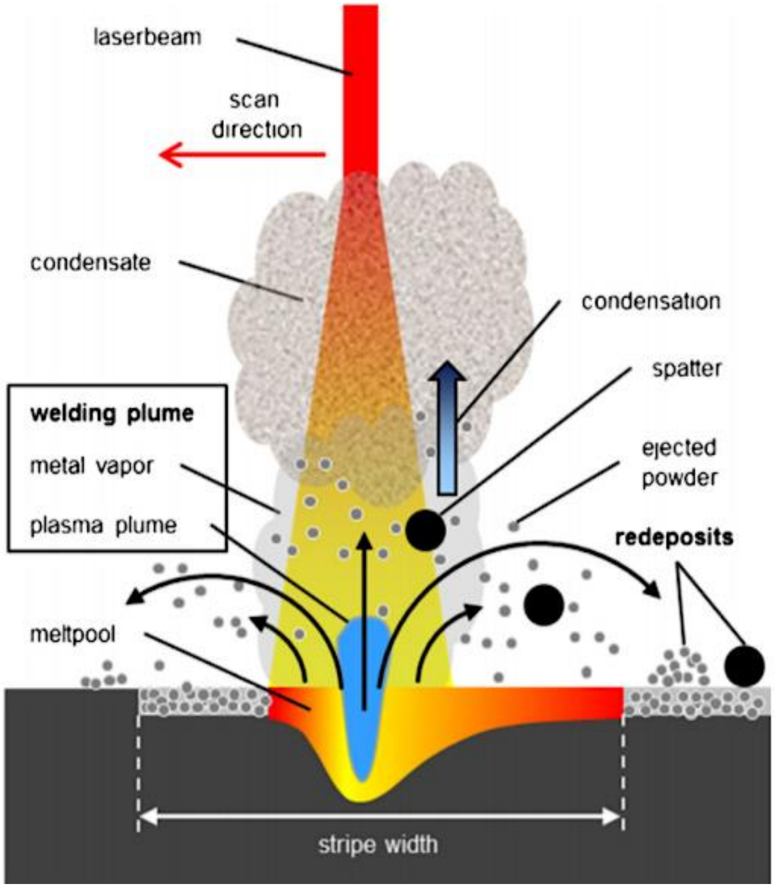

Figure 1.2: Dynamics of laser powder bed fusion at the interface between the laser and powder. Note the development of spatter and condensate from molten metal. [3]

Using the EOS M290 LPBF system as an example, the inert gas is introduced from the back of the build chamber via two inlet nozzles, one near the top of the volume and one near the build plate (Figure 1.3). After passing across the build chamber from the back to the front, the inert gas stream is directed to an exit baffle located at the front of the build chamber. The exhaust gas is then directed into a filter cabinet where it passes through a multi-step filter cartridge intended to collect any condensate. The argon is continuously recirculated until the build is complete.

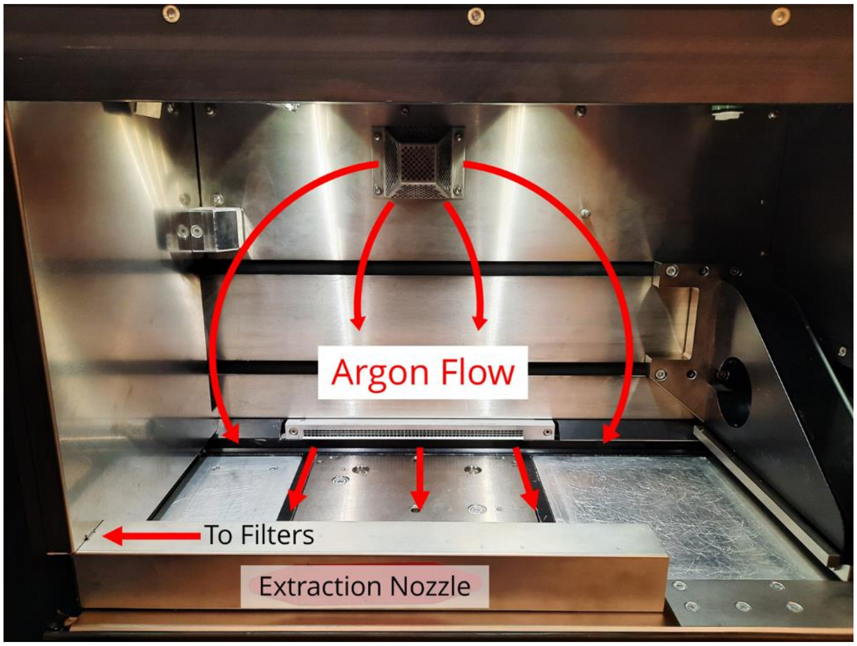

Figure 1.3: Diagram of gas flow in the EOS M290 build chamber as viewed from the access door. Photo courtesy of Alex Montelione.

If the gas flow within the build chamber is not uniformly distributed or there are attributes of the gas flow that interfere with the powder bed or the evacuation of metal vapor condensate, the quality of metal produced could be degraded in the affected areas. There is substantial concern within the metal AM community that the gas flow within commercial LPBF systems is not adequately controlled and that it contributes to the generation of defects and/or inconsistent mechanical properties of components from across the build area [5]. These inconsistencies in metal quality across the build plate lead to difficulties in creating material design values that can be applied in an industrial setting. According to Troy Haworth of the Boeing Company, “Using separate design values for different regions of the build plate would increase the cost and complexity of developing components with LPBF.” Therefore, a quantitative evaluation of the gas flow distribution within the build chamber is essential to the manufacture of metal components by LPBF with the maximum degree of quality and reliability.

Previous investigations have been performed to analyze the flow conditions in LPBF systems using Computational Fluid Dynamics (CFD) [6]. In addition, a particular effort that precedes the current investigation was performed that involved the design and manufacture of a mock build chamber and adopted Particle Image Velocimetry (PIV) to characterize the inert gas flow field experimentally [7]. Although that preliminary investigation resulted in the creation of the experimental apparatus and simplified flow models, further investigation using more developed PIV techniques at different sections of the build plate is necessary, as the results were inconclusive with the behavior of the inert gas. The critical next steps should be focused on refining the experimental system and performing gas flow analysis experiments that help establish a more thorough understanding of the spatial and temporal variability of the gas flow in the EOS M290.

1.4 Objectives

Based on the importance of understanding the inert gas flow distribution within the build chamber of commercial LPBF systems, as well as the developments of previous capstone teams in establishing a viable approach for this pursuit, an experimental investigation was performed. The primary objectives of this investigation are the following:

- Further develop and refine an experimental approach to characterize the inert gas flow within the build chamber of an EOS M290 and selected regions of the build volume using Particle Image Velocimetry.
- Through the application of PIV, develop quantitative descriptions of the gas flow and identify locations in the build chamber where the gas flow distribution exhibits

undesirable characteristics and/or that could contribute to the development of build defects and poor part performance.

- Evaluate the flow field within regions of interest using 2- dimensional velocity measurements and determine if a 3-dimensional analysis is warranted.
- Provide quantitative understanding that can inform the design of new nozzle geometry or ducting system components for the EOS M290 LPBF system to improve the gas flow distribution for improved part quality

Chapter 2 LITERATURE REVIEW

Metal AM has been the focus of considerable research and development efforts due to several perceived advantages over traditional manufacturing processes [8]. In the aerospace and biomedical industries where stress-critical and safety critical applications are more common, LPBF of titanium alloys has become of topic of substantial interest [9, 10]. Relevant to the applications of LPBF in general, and the manufacture of stress-critical components in particular, there has been recognition of the need for understanding contributions to the metal quality and its variability. The primary focus in these investigations have been on determining causes to anisotropy and mechanical property variability [11], whether it be due to the powder feedstock [12], or the effect of laser parameters [13]. In support of these efforts, methods of in-situ monitoring have been investigated with the goal of developing techniques that recognize the introduction of defects as they occur, or that can repair them during the build process.

One of the current concerns in the industrialization of LPBF is the variability in mechanical properties of components that result within a machine and across machines [14-17]. Recent investigations have questioned the role of the inert gas distribution in the build process and its potential contribution to the development of defects, as further discussed in Section 2.4. Prior to reviewing studies on gas flow, it is important to discuss the defects that can develop in LPBF, contributing mechanisms, and their influence on properties.

2.1 Common Defects in Laser Powder Bed Fusion

There are several types of defects that commonly occur in the LPBF build process. Any defect that changes the overall density of the build has the potential to cause a reduction in the structural integrity and strength due to the stress concentration posed by the void. Edwards and

Ramulu [18] were among the first to investigate how porosity effects the fatigue performance of Grade 5 Titanium components printed by LPBF, among other issues.

The three most common defects in LPBF of metals includes gas pores, lack-of-fusion voids and key-hole defects [19]. Key-hole defects are among the most detrimental and arise due to the displacement of powder in the laser melt process under excessive laser intensity and low scan speeds [20]. Once the laser has passed by a powder region that has been excessively melted, the powder collapses on the defect and leaves a bubble which contributes to part porosity. Wang et al. conducted simulations to model the formation of keyhole defects and compared the results to experimental data [21]. Their results indicated that lower ambient pressures reduced the occurrence of keyhole pores due to the reduced recoil pressure from the laser interacting with the powder bed. It was also found that a slight increase in scan speed could decrease the pore sizes significantly. Wang also noted that keyhole defects have been shown to be directly affected by condensate and vapor plumes within the build chamber, which should be removed by proper gas flow.

Jakumeit et al. conducted simulations of the melt pool dynamics and verified its influence on part porosity with additional support from experimental data [22]. Bitharas et. al [23] conducted Schlieren imagery of vapor plumes with different scan speeds and energies and demonstrated that keyholing was directly attributed to excess energy density resulting in greater melt pool instability. The inert gas flow and its uniformity appears to be important to the development of keyhole defects.

Lack-of-fusion (LOF) voids are another major class of defects in LPBF, which are generated when the laser scan does not fully melt the layer of powder, and results in a region of non-contiguous metal between two adjacent layers. These defects are usually associated with insufficient laser power and incorrect (excessively high) scan speeds [24]. Mukherjee and DebRoy [25] developed a fluid flow and heat transfer model of the laser melt process to predict the formation of lack-of-fusion defects. They developed a non-dimensional number to quantify the proportional effects of scanning speed, layer thickness, and hatch spacing with the inverse effects of laser power. Results of their work showed that lack-of-fusion defects were found to largely depend on the melt pool shape and size, which as outlined by Ladewig [3] can be affected by attenuation of the laser beam due to condensate. Further efforts utilizing synchrotron-based micro-tomography were pursued by Gordon et. al [20], resulting in the development of Defect Structure Process Maps (DSPM) to quantify porosity in LPBF manufactured components based on processing parameters, melt pool data, and melt pool depth.

It is important to highlight that the methods outlined in this section for evaluating defects in build metal are entirely ex-situ monitoring processes utilizing techniques like MicroCT, SEM, or other measurement techniques. In-situ process monitoring of the build does not directly detect defects as they form but can help to establish the root causes and signatures of their development. But even when considering existing ex-situ and in-situ approaches for evaluating the build process and its products in LPBF, these approaches cannot provide a clear understanding of the gas flow distribution within the build chamber and whether it contributes to the development of metal defects. A direct measure of the gas flow is necessary.

2.2 Metal Vapor Condensate

One of the primary causes of keyhole and LOF defects is the accumulation of metal vapor condensate (MVC) and its interference with the incident laser [20]. In general, MVC is generated by the vapor plume that results from the intense heating in laser-powder interactions and the resolidification of metal vapor while suspended above the powder bed. The initiation and growth of condensate within the build chamber occurs via processes such as oxidation, coagulation, and agglomeration [23]. Condensate has been shown to attenuate the incident laser beam by interfering with the path of the laser before it reaches the powder bed [26]. That attenuation can lead to defects such as lack-of-fusion, and increased surface roughness [3, 27]. Ferrar et al. characterized the amplifying effect of condensate on porosity and reduction in compression strength of printed titanium specimens [28]. They postulated that the regions of higher condensate concentrations were also areas that suffered from weaker and less uniform inert gas flow.

From these findings it becomes clear that the vapor plume formed in the rapid melting of powder by laser irradiation has a detrimental effect on part performance. Furthermore, an effective/uniform inert gas flow is critically important to the production of high quality metal. It is therefore necessary to ensure that LPBF systems have well designed gas flow systems. As such, characterization of the gas flow is a recommended step to assess its uniformity across a build surface and address factors that could potentially sacrifice metal integrity and part performance.

2.3 **Process Monitoring**

In situ monitoring of the build has been pursued by many research teams to examine the development of defects in real time, to understand the root causes of these defects, as well as to prevent build anomalies or even build failure. EOS has developed EOSTATE, which is a suite of in situ tools that have been developed to record system parameters during a build such as atmosphere composition, laser power, and temperature. Part of the EOS suite of monitoring tools is EOSTATE Powderbed, an optical system that takes a snapshot of the print bed after recoating and after the laser scan is complete. Another monitoring tool within EOSTATE is EOSTATE MeltPool, which optically monitors the melt process at wavelengths between 400 nm to 900 nm. MeltPool operates with two photodiodes near the laser scanner, allowing complete spatial and temporal collection of light transmission from the melt process. Finally, there is EOSTATE Exposure OT (Optical Tomography), which, in conjunction with machine learning, records long-exposure images with a scientific CMOS camera in the near infrared range (900 nm) to ascertain areas of high heat transfer that may indicate areas of high thermal stresses, and potential regions of concern in the printed part.

Substantial research has been conducted on the methods of process monitoring employed by EOSTATE and others, as well as their effectiveness. The most common method of in-situ monitoring is by a layer wise approach. Optical methods in conjunction with thermal monitoring have been developed by Yuan et al. to perform in situ monitoring of the melt track dimensions [29]. They developed a methodology with machine learning algorithms for determining deviations in the melt pool width and their effects on material performance through the construction and use of a library of training data of melt track width measurements [29]. Lu et. al devised a system utilizing optical cameras and image recognition to determine part density based on features of printed test specimens. Through an experimental evaluation involving printing of 316 L stainless steel, they found a direct correlation between the melt track dimensions and part density with the yield strength [30]. Feng and Chen et. al developed methodology utilizing optical tomography to predict defect generation utilizing machine learning [31]. Dunbar et al. captured in-situ measurements of temperature and metal distortion introduced using different scan patterns. Their apparatus utilized a thin substrate with a micro-strain gauge and thermocouples in two locations. The substrate was prepared with a layer of powder distributed over it, and then a build layer is formed on top through melting of the powder. Interestingly, their results showed that a constant scan pattern resulted in greater distortion than a rotational scan pattern [32].

Acoustic monitoring of the build process has also been pursued in conjunction with machine learning by collecting acoustic signals during the builds, and comparing the acquired signatures to a library of acoustic signatures that are indicative of defect generation [33]. Similarly, Pandiyan et al. utilized machine learning to enhance process monitoring involving the collection of acoustic signatures [34].

As evident from the cursory review of in-situ monitoring methods in this section, past research has been primarily focused on parameters pertaining to the powder/laser interaction, with complementary focus on the implementation of machine learning to pursue optimized evaluation and control schemes that can improve or ensure part uniformity. Unfortunately, to the author's knowledge, it is not possible to evaluate the gas flow dynamics during the build process through the application of in-situ monitoring tools. Although in-situ monitoring tools can be used to study the development and presence of defects, it would be impossible to identify if characteristics of the gas flow distribution are the root cause. Furthermore, there has been relatively limited scientific focus on the inert gas flow, which makes this a fruitful area for research and the development of new knowledge.

2.4 Inert Gas Flow in LPBF

Non-uniform gas flow across the build plate can lead to areas of the build that have increased interference from the plume of metal vapor condensate. Bitharas et. al. conducted schlieren and x-ray photography of the vapor plume and its evolution to characterize the plume as it passes over defect areas. Their hypothesis was that it may lead to an amplification of the defect. They presented experimental data (Figure 2.1) consisting of a series of schlieren photographs with and without gas flow that highlighted the importance of gas flow in managing the vapor plume and reducing laser attenuation [23]. Without inert gas flow, it was found that the vapor plume was enlarged and very chaotic in comparison to conditions with gas flow. The primary cause was a lack of forced convection that promotes heat transfer and reduced attenuation of laser power by scattering of the laser beam.

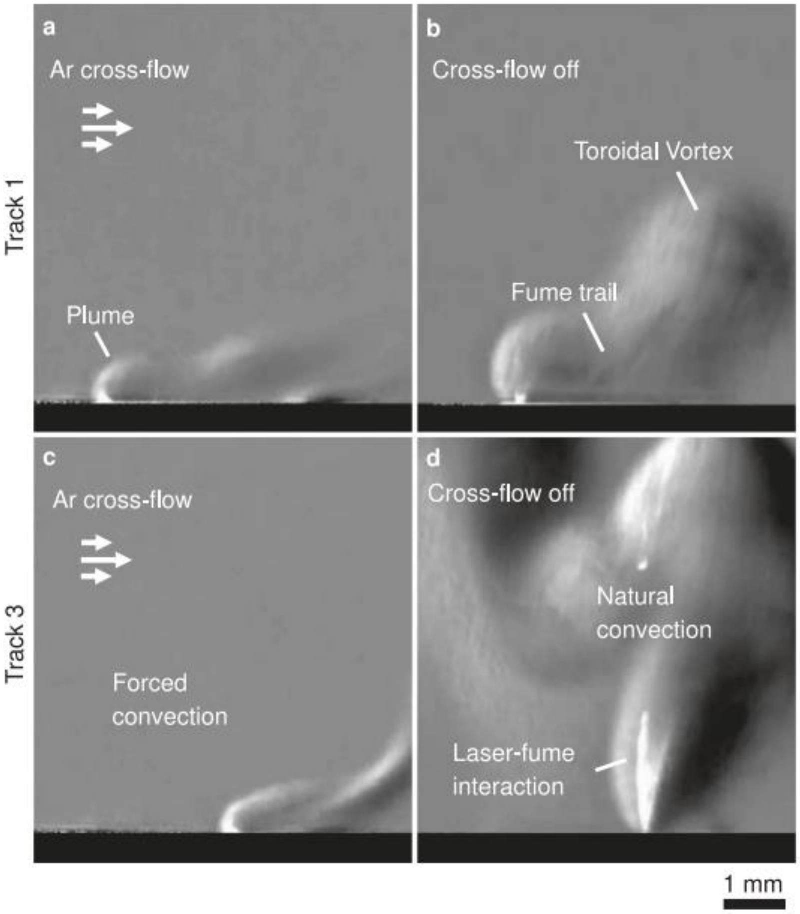

Figure 2.1: Effect of gas flow on vapor plume formation in two separate locations. Parts a) and c) show the attenuated plume development when the gas cross-flow is on, and b) and d) show the amplified plume development that is formed when the cross flow is off. [23].

Reijonnen et al. investigated gas flow in LPBF utilizing hot wire anemometry within the build chamber of a commercial printer (SLM 125). A schematic diagram of the hot-wire distribution in the build chamber is shown in Figure 2.2. Their findings highlighted that the recoater position affects local gas flow, which should be considered in any evaluation of gas flow within a build chamber. Additionally, Reijonnen et al. also compared the metal microstructure to the gas flow distribution and found that regions of the build plate with lower flow speeds corresponded to higher porosity [5]. Philo et al. also conducted hot wire anemometry to verify CFD simulations of the gas flow distribution inside a Renishaw AM250. Interestingly, they developed new nozzle geometries to improve flow uniformity [6].

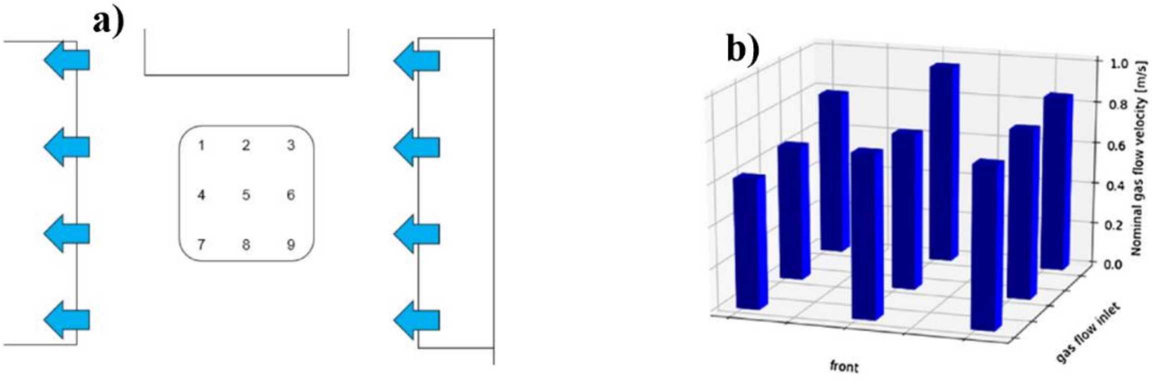

Figure 2.2: Evaluation of gas flow within a SLM 125 by Reijonen et al. a) hot wire experimental arrangement. The numbers 1 to 9 correspond to anemometer positions evaluated in a SLM 125. b) measured gas flow at each position with flow at 4 m/s at the inlet [5].

Weaver et al. [35] also investigated gas flow utilizing hot wire anemometry, but within an EOS M290, the same machine that is the subject of the present investigation. Their investigation was conducted with nitrogen gas at a flow differential pressure setting of 58 mbar. They compared two lower inlet designs provided by EOS, including the one that was utilized in this investigation. The EOS M290 has two inlet vents, one near the roof of the build chamber (upper inlet), and one closer to the print bed (lower inlet) as shown earlier in Figure 1.2. Data collection was obtained in all three axes of the build chamber, and interpolated heat maps were generated to visualize the flow dynamics throughout the build volume (Figure 2.3).

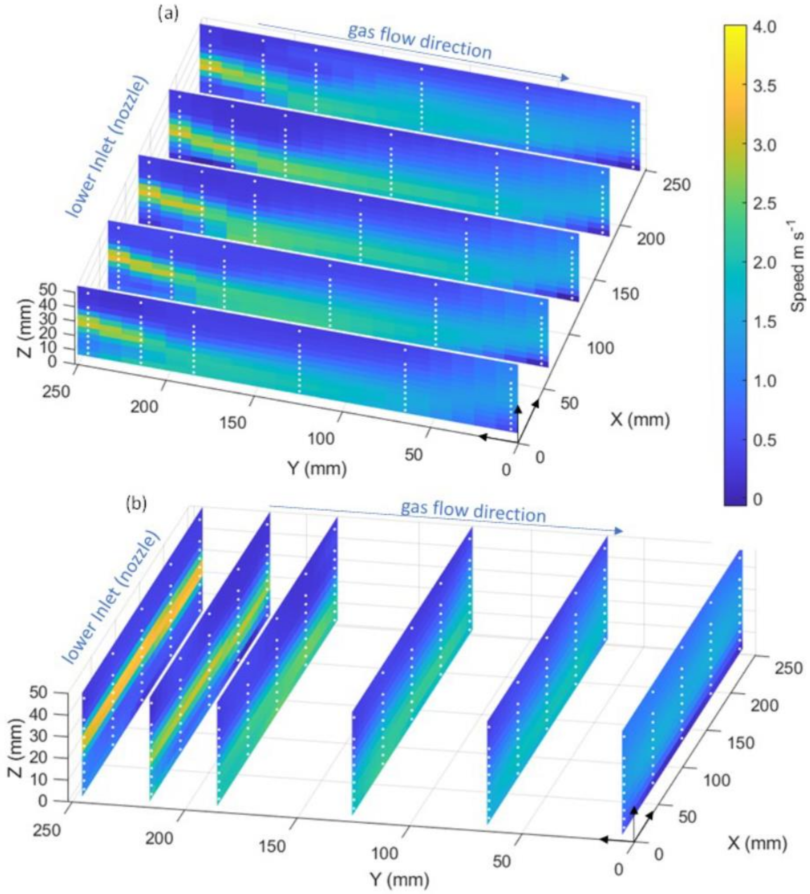

Figure 2.3: Interpolated maps of the gas flow velocity obtained from Hot-Wire Anemometry. These results are from Weaver et al. using Nitrogen as the inert gas with the standard lower inlet nozzle. [35].

Overall, their findings suggested that the gas flow in the EOS M290 is non-uniform. Interestingly, they concluded that the gas flow is deflected downwards from the lower vent and exhibits non-uniformity across the build plate. They also noted a decrease in flow velocity after it exits from the lower inlet. Their results indicated that the velocity profile is uniform across the lower vent vane and across the build plate (the x-axis), which will be discussed later in this thesis. Although this study provided new understanding of the gas flow distribution within the M290, the coarse nature of the anemometer measurement grid is unable to elucidate the finer details regarding the transient flow characteristics and localized variabilities. Additionally, hot wire anemometry does not account for the flow direction, only its magnitude in the direction the probe is pointing. These limitations establish the importance of adopting alternative measurement techniques with higher fidelity.

Bidare investigated the variation of atmospheric pressure and composition (helium vs argon) in the build chamber and determined that particle entrainment in the flow field was reduced with increasing gas pressure for either gas environment [4]. Although an increase in pressure also reduces the chance of spatter in both compositions, this effect was attenuated for argon. With argon, it was determined that higher atmospheric pressures increased the generation of spatter due to the increased vaporization temperature of the melt pool. These undesirable characteristics that resulted with higher gas pressure were not observed with helium, which was hypothesized to be caused by its higher conductivity relative to argon. Amano et al. [36], also investigated the influence of different gas atmospheres on the extent of generation of spatter. Their results indicated that a helium atmosphere was superior to argon in reducing spatter, potentially due to its higher thermal conductivity and lower density. Additionally, it was shown that the degree of spatter increased with increasing oxygen concentration, highlighting the importance of ensuring that the atmosphere in the build chamber is adequately inert.

Li et al. [37] investigated the effects of atmospheric pressure in LPBF utilizing numerical methods and verified their findings with high-speed x-ray imaging. Their results agreed with those of Bidare [4], which showed that an increase in atmospheric pressure reduced powder entrainment. Investigations by Traore et al. have also been performed concerning the composition of the inert atmosphere and its effects on builds involving Ni-based alloys [38]. Although the track dimensions were found to be consistent with argon and helium atmospheres, the spatter was lower in the helium experiments, particularly at higher energy densities. But since Helium is typically more expensive than argon per unit volume, argon remains the most used noble gas [38].

Considering the higher end of the gas flow spectrum, Shen et al. [39] investigated the upper limit of gas flow velocity with respect to powder size and developed a model for powder-pickup with respect to the inert gas composition, powder morphology, and powder composition. If the gas flow is too high, powder may be displaced or removed from the build surface, thus leading to uneven layers, which may cause keyhole defects or lack-of-fusion. Therefore, while most of the current focus in research on gas flow is directed on the lower limit of velocity, it is important to acknowledge that an upper limit does exist, which is dependent on the powder morphology and density .

Perhaps more relevant to the work performed in the present investigation, Particle Image Velocimetry (PIV) has been applied to characterize gas flow within a mock-build chamber of an unspecified SLM printer, which has a very different configuration from the EOS M290 [40]. That study was focused primarily on vent geometry design and its optimization. Specifically, the activities of that investigation were directed towards determining stagnation locations in the flow field and methods for adjusting its position utilizing new nozzle designs. Figure 2.4 shows the variation in velocity across different regions of the build chamber, which facilitated an evaluation of the flow in two spatial dimensions. The team reported that PIV was useful in measuring areas of stagnation and in determining the effectiveness of changes in nozzle geometry.

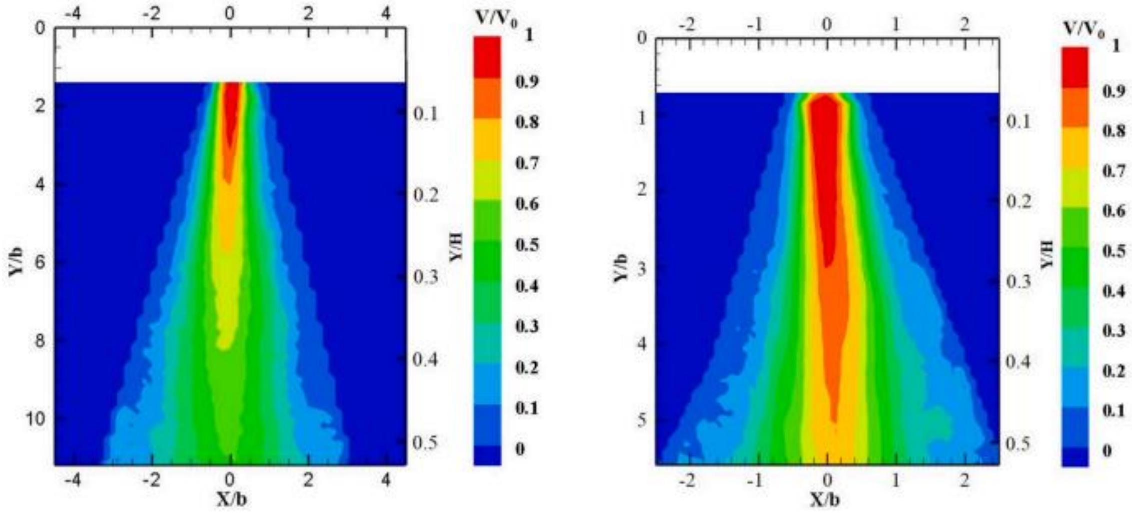

(a)

(b)

Figure 2.4: PIV results from Chen et al. [40] in a region of their mock build chamber comparing between two different nozzle geometries, a) higher aspect ratio and b) lower aspect ratio.

Also of relevance, Elkins et al. [41] recently employed Magnetic Resonance Velocimetry (MRV) to model the three-dimensional flow in a 1/3rd scale model of an EOS M290. They utilized water as the fluid medium at Re = 36000. Their results showed that the flow field exhibited a non-uniform velocity distribution, with the velocity profile varying in all axes, and an area of backflow near the lower inlet. The maximum velocity recorded was 4 m/s and developed near the center of the lower vent, which will serve as a source of comparison with the results of the present study. Although the team was able to make an important contribution, the major limitation of MRV is the high cost of conducting the experiments. It requires the use of an MRI machine to capture the movement of the magnetic flow particles to support quantification of the flow fields via cross correlation. Nevertheless, the MRI approach supports a complete 3D visualization of the mock build chamber. The previous work performed using PIV is limited to evaluating flow across 2D slices of the build space in regions of interest. It is not clear if a three-component evaluation of the flow field is necessary, which is one of the questions that will be addressed in this investigation.

2.5 Summary

Due to many advantages of LPBF for near-net shape manufacturing, it is being sought for applications in aerospace. The performance requirements of aerospace structures has led to considerable research to understand the defects generated in LPBF of metals, including Ti6Al4V, and their effects to the metal quality and mechanical properties. The efforts focused on characterizing defects and their generation have provided a classification of defects in LPBF. Overall, the vapor plume and condensate generated by laser-powder interactions are primary contributions to development of voids. In addition, due to the importance of these defects to metal quality and part durability, various methods have been applied for in-situ monitoring of the build process. The ultimate goal of these efforts is to pair the collected data with the machine's build software and machine learning algorithms to identify defects as they are generated to perform non-destructive inspection.

Additional research has been conducted to understand effects of the inert gas atmosphere in the build chamber on the generation of defects and mechanical properties of the metal, including spatial variations. While the gas atmosphere is important (i.e., argon vs helium), the atmospheric pressure and gas flow velocity have been identified to be key contributors to spatter generation. Furthermore, both computational and experimental methods have been applied to understand the gas flow distribution within the build chamber. And based on the technologies available, PIV appears to be a powerful approach for analyzing the gas flow distribution in LPBF systems. However, no study has applied PIV to understand the gas flow distribution within the

EOS M290 and distinguish zones of concern or performed a 2D or 3D flow analysis “at scale”. Therefore, an investigation of the inert gas flow within the build chamber of the EOS M290 is warranted and could provide new understanding that supports process improvements.

Chapter 3 MATERIALS AND METHODS

An experimental investigation was conducted to evaluate the gas flow distribution within the build chamber of the EOS M290. This chapter describes the materials and methods that were used to develop a system enabling a robust evaluation of the flow field within the build chamber utilizing Particle Image Velocimetry (PIV) and a quantification of spatial variations in the gas flow distribution of interest.

3.1 Mock Build Chamber Design

It is important to highlight the potential contamination issues and undesirable nature of any modifications that would be required to conduct flow visualization experiments within the build chamber of a fully operational M290 machine. Therefore, rather than conduct the experiments within an actual EOS M290, a model of the build chamber was constructed to enable an independent study of the gas flow distribution without affecting the build schedule. That approach prevents contamination of the EOS M290 caused by any visualization methods, and avoids the need for modifications to accommodate flow field visualization.

A model of the build chamber for the EOS M290 was designed by engineers of the Boeing company to dimensionally match the build chamber inside the machine. The digital model was then used to construct a physical model that was performed by a Boeing-UW capstone team [7]. The system consisted of a 1:1 scale model of the build chamber and plumbing system as shown in Figure 3.1

The first iteration of this “mock” build chamber (MBC) was made primarily of 13 mm thick sheets of plexiglass, to allow visualization of the flow field through the walls. In addition, the system utilized the nozzle inlets and outlets from an actual EOS M290. The inlets used in the

MBC were original equipment parts from an EOS M290 system and were placed in their corresponding positions. The inlet gas flow design is important to note, as it incorporates an original equipment Y-Duct, which is produced by Selective Laser Sintering (SLS) with internal ribs that extend throughout its length. The Y-Duct geometry separates the flow into two components that are delivered to the lower and upper inlet nozzles at the back of the machine as shown in Figure 3.1.

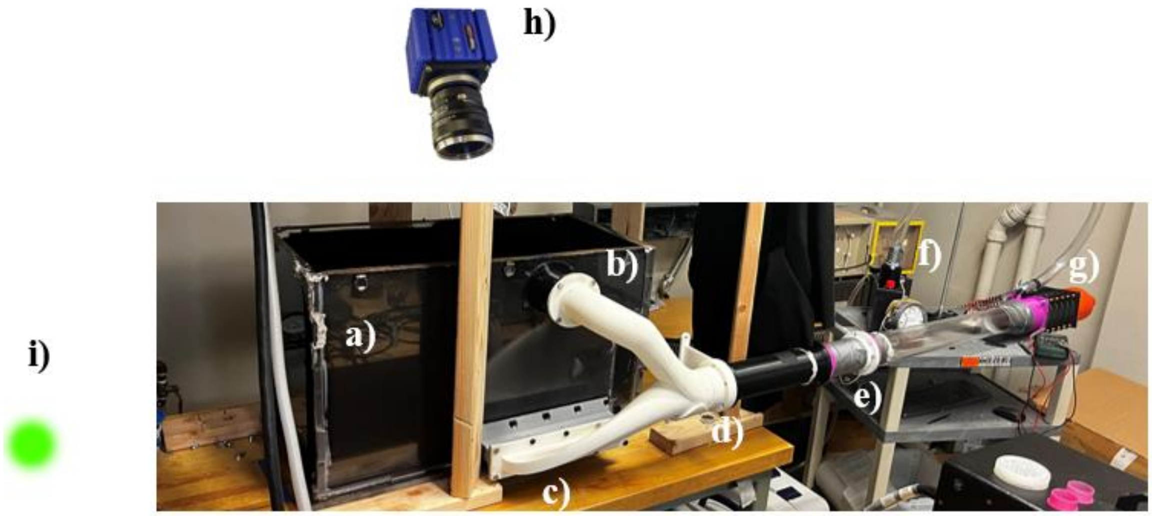

Figure 3.1: Mock build chamber ducting system. Key components include a) Mock Build Chamber (primarily plexiglass, with flocked paper in interior to aid in reflection reduction during experiments), b) upper inlet of Y-Duct, c) lower inlet of Y-Duct, d) Y-Duct entrance, e) differential pressure gauge probe, g) seeder, g) fans, h) LaVision CMOS CLHS camera [42], i) Evergreen 200 laser.

The lower inlet vent appears to have been designed to encourage uniform flow from the lower inlet nozzle and straight across the build plate to reduce recirculation. Similarly, the top inlet vent has been designed with a straightener as well. Its primary purpose is to prevent condensate and smoke from recirculating in the build space and from clouding the laser lens located at the top of the machine. The outlet vent is positioned on the opposite side of the build chamber from the inlets, at the front of the machine, and extends along the width of the build plate. The outlet vent (Section c in Figure 3.1) has a series of slanted baffles that serve to guide the gas flow through an exhaust pathway.

3.2 Gas Supply Design

All gas flow experiments in this investigation were conducted utilizing air in place of argon, which was justified for this evaluation by matching the Reynolds number ($Re \approx 39000$). The inlet flow speeds in this experiment were targeted to match those obtained from the volumetric flow measurements in EOS M290 machines, which was verified with a vane anemometer. The inlet volumetric flow rate for the EOS M290 was measured using an anemometer custom-made by The Boeing Company and was determined to be 120 m^3 /hr. That volumetric flow rate correlates to a velocity in air of approximately 7.2 m/s at the entrance to the Y-Duct, with a corresponding Reynolds Number of $Re = 39000$. The inlet velocity to the MBC was measured/verified in the apparatus utilizing a differential pressure gauge, like the flow measurement method utilized by the M290. The pressure gauge had one probe read the static conditions in the flow, and the other read the total pressure at the center of the stream. By getting the difference between these two values, the dynamic pressure, and therefore velocity of the gas can be determined. Air was circulated in a closed loop system utilizing a series of inline fans and the differential pressure gauge was placed downstream (Figure 3.2 & Figure 3.3). The fans were powered by a dedicated 120 W, 12 V power supply, and the voltage was controlled by a potentiometer in a boost converter board.

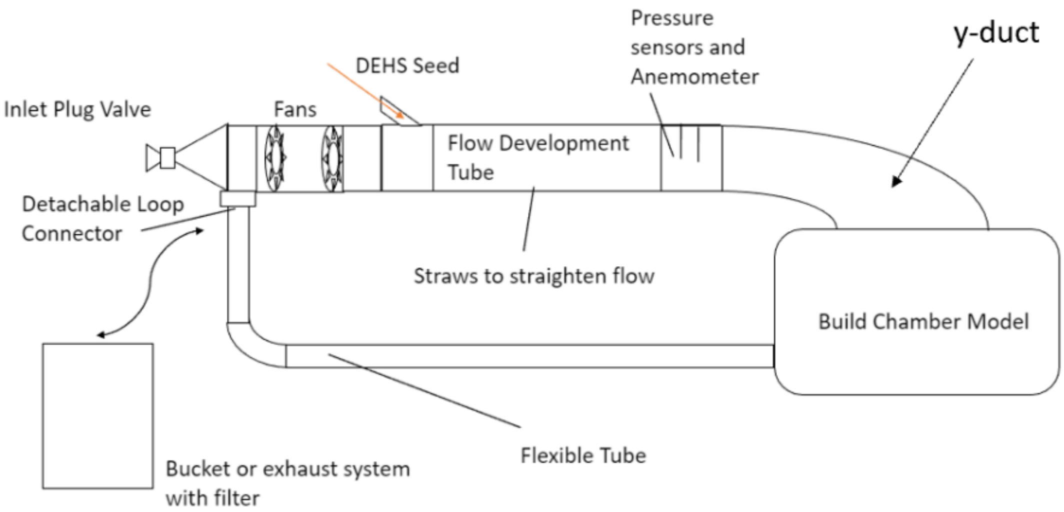

Figure 3.2: Schematic diagram of the gas supply system used with the mock build chamber [43].

To apply PIV it was necessary to seed the air flow with particles to visualize the flow field. Seeding was conducted utilizing Di-Ethyl-Hexyl-Sebacate (DEHS) atomized with a commercial atomizer (Model 9306, TSI Six-Jet Atomizer, Shoreview, MN) and with pressurized air serving as the injection gas. Recirculation of the seeded gas flow that exited the outlet baffle was achieved by a fluid circuit that involved 3D printed connectors produced using Fused Filament Fabrication (FFF) and off-the-shelf flexible tubing. One of the printed connectors was designed with a side inlet for the injection of DEHS as shown in Figure 3.3. The DEHS was propelled by pressurized air at 69 kPa (10 PSIG). Based on the images acquired by PIV, the DEHS was fully atomized prior to reaching the inlet nozzles to the mock build chamber.

Early iterations of the experimental routine utilized an in-line vane anemometer upstream of the Y-Duct, which enabled verification of the differential pressure gauge measurements and to account for inclusion of the seeder. After measurements of the gas flow were verified and before experimentation began, the vane anemometer was removed due to redundancy with the differential pressure gauge and the obstruction caused by the vane. According to calculated results informed by the anemometer and inclusion of the seeder at 69 kPa, the target measurement from the differential pressure gauge was 32 Pa [0.13 inWC].

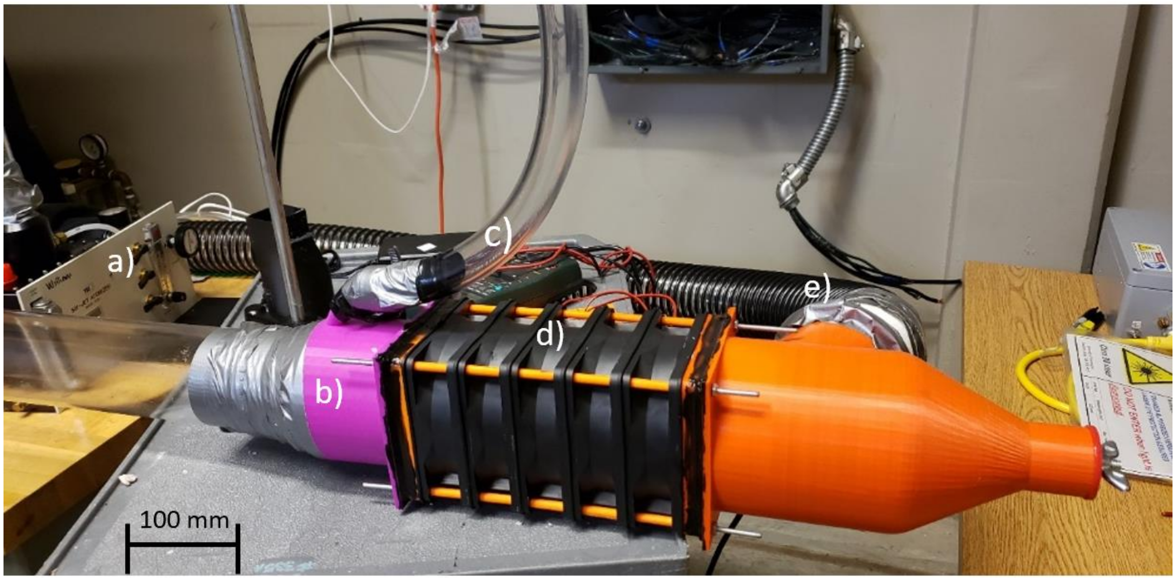

Figure 3.3: Supply fan apparatus and seeding. a) the DEHS seeder, b) DEHS injection point, c) DEHS injection tube, d) series of fans, e) recirculation point. Original image from [43].

3.3 PIV Hardware & Software

The PIV system using in this investigation is a commercial unit produced by LaVision GbmH, which includes a laser for illuminating the particle distribution, a camera for imaging of the particle movement and the PIV software for acquiring images and conducting post-processing to generate the flow fields. All experimental evaluations performed in this investigation were conducted in planar view with one camera, as opposed to stereo view with two cameras. Planar (i.e. 2-dimensional (2D)) evaluations could be conducted with the laser plane oriented normal or parallel to the gas inlet. The evaluation began by viewing the mock build chamber from the right side relative to an operator, which provides a two-dimensional view of the YZ plane (YZ Planar View) as shown in Figure 3.4.

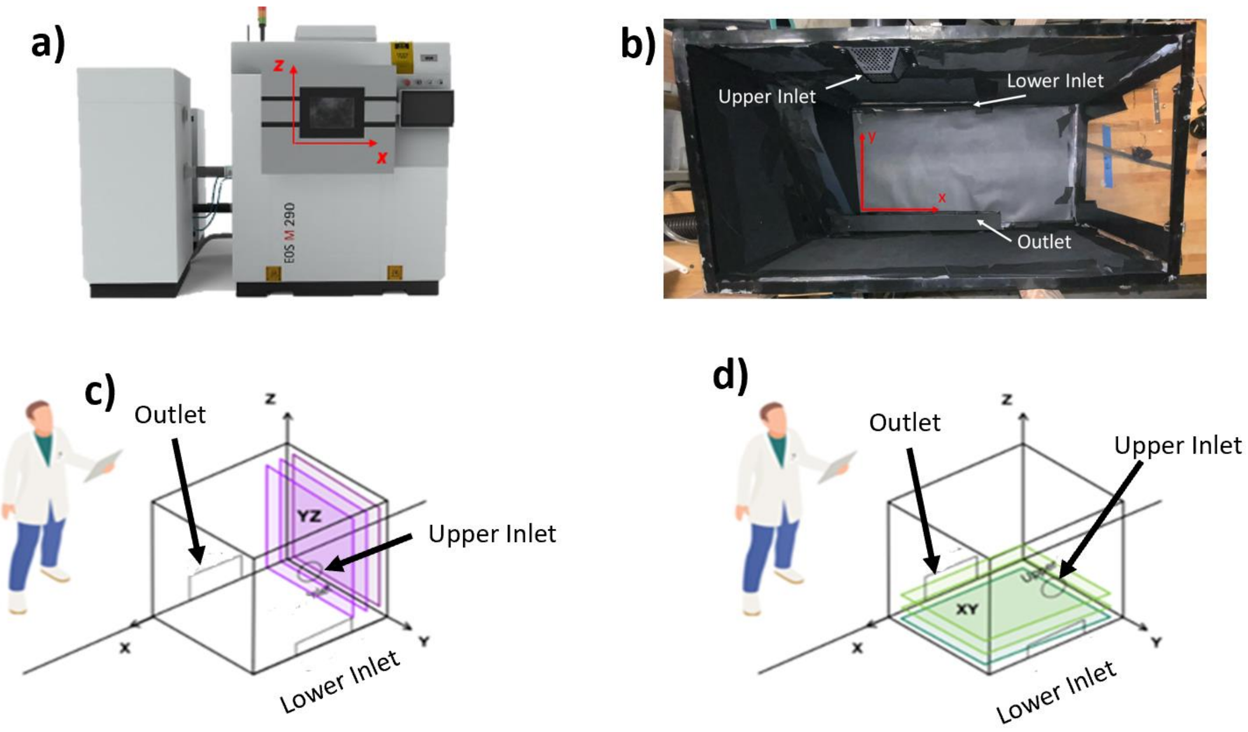

Figure 3.4: Location of origin in a) the EOS M290 from the point of view of an operator, b) the Mock Build Chamber viewed top-down, and orientations of c) YZ planes and d) XY planes in the Mock Build Chamber. Image courtesy of Yobel Abraham.

Illumination of the flow field was achieved by a Class IV Evergreen 200 Dual Pulse Nd:YAG laser, with wavelength of 532 nm. Power and water cooling of the laser was provided by its power supply/water pump unit. Control was communicated between the PC and LaVision Programmable Timing Unit (PTU) to the power supply. The PTU served to synchronize and time the laser pulses with the captured images from the camera. A Scheimpflug adapter was used as a lens mount even though it is customarily not required for Planar PIV. The adapter caused a slight increase in focal length. A complete schematic description of the instrumentation and communication is given in Figure 3.5. The camera used in the PIV arrangement was a LaVision Imager sCMOS CLHS (Göttingen, Germany) with 5.5 Megapixel resolution. Nikon lenses with focal lengths of 50 mm and 60 mm were utilized in the experiments in conjunction with the sCMOS cameras. Images collected by the camera were collected via fiber optics to a frame grabber onboard the PC, where it was then recorded by the LaVision DaVis software.

Due to limitations in lens quality at lower focal lengths, it was necessary to balance the window of evaluation dimensions with image quality. As a result, it was not possible to capture the entire build envelope in the planar views. Early preliminary experiments were conducted with a wider field of view (FOV) that were enabled by lenses with smaller focal lengths (e.g. f = 35 mm). However, these efforts were not successful due to the seeder particles appearing too small. Further information regarding the PIV system parameters is provided in Appendix I. For the f = 60 mm and f = 50 mm lenses, the calculated angular FOV was 15.7 degrees and 18.9 degrees, respectively.

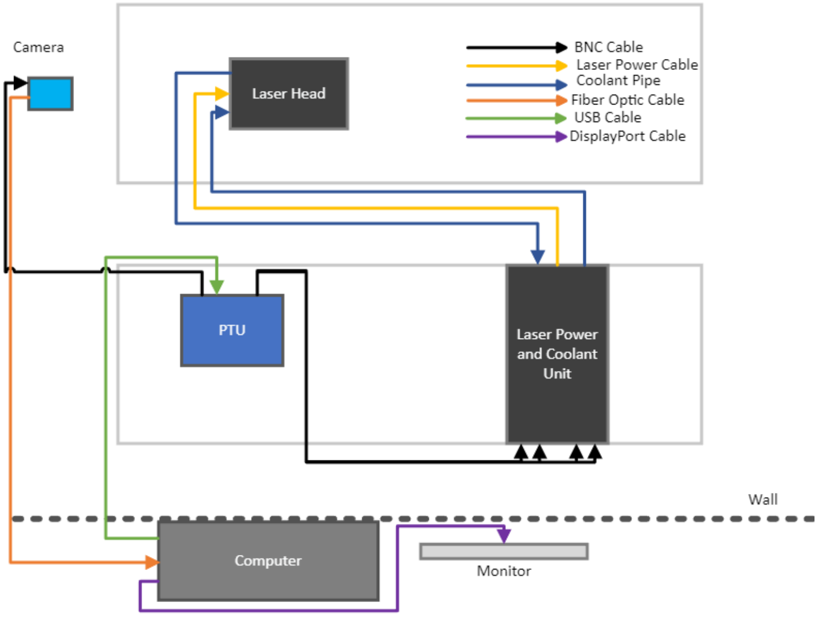

Figure 3.5: An instrumentation diagram for the experimental setup. Original image from [43].

For the YZ planar views, the laser was mounted above the mock build chamber with an enclosed 90-degree mirror and the camera was mounted to face the right side of the mock build chamber as shown in Figure 3.6. A divergent optic with a focal length of 10 mm was utilized with the LaVision Light Sheet Optic to produce a laser sheet that enveloped the cross section of interest of the Mock Build Chamber. To obtain the XY views, the positions of the camera and laser were switched, with the laser emitting the laser sheet from the side of the build chamber (Figure 3.6), and the camera point of view from above; the 90-degree mirror was not necessary for the XY views. The camera utilized a 50 mm lens.

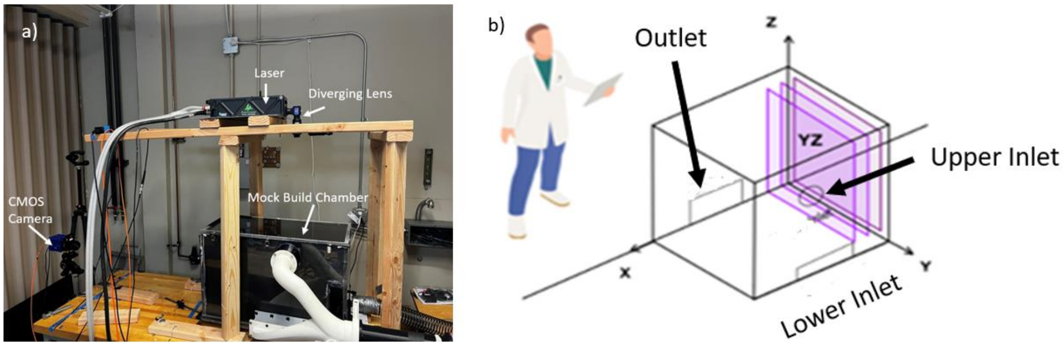

Figure 3.6: a) PIV experimental arrangement for planer analyses in the YZ orientation and b) planes of evaluation in the Mock Build Chamber.

A calibration was performed to ensure that the dimensions of the documented space resulted in accurate measures of the flow velocity. The process was conducted utilizing a calibration plate (Model 204-15 Calibration Plate, LaVision, Göttingen, Germany). The calibration plate was positioned to be within a few mm (+/- 4 mm) of the laser sheet position. After positioning was determined, the chamber was illuminated with a high-lumen work light and the camera was turned on. The camera was positioned into place, utilizing the calibration plate as a reference in the frame. Thereafter, the camera lens was focused on the calibration plate until a crisp image was generated and visible on the viewing screen of the DaVis software and a snapshot was taken. The DaVis software then computed the pixel-to-mm ratio using a dot-search algorithm based on the stored values for dot spacing of the plate. The average calibration fit error was estimated to be approximately 0.6 pixels, which was largely attributed to refraction caused by the thick plexiglass used in the construction of the build chamber. After completing calibration, the calibration plate was removed, and the mock-build chamber was sealed. Thereafter, neither the mock-build chamber nor the camera was moved after calibration was completed, or the calibration process would need to be restarted.

The laser sheet position was adjusted by either moving the mock-build chamber assembly along the x-axis for the YZ plane analysis, or by shifting the box or laser system along the z-axis for the XY plane analysis. Camera positioning was performed with consideration of the field of view (i.e. the visible cross-section) and to minimize the effects of reflections. Calibration was conducted each time the box or camera was moved. The adverse effects of reflections on data collection were reduced by physical masking of surfaces to disrupt reflected light and by digital masking using post processing tools. In addition, adjustments to the mock build chamber and other hardware were performed to diminish other potential undesired light sources.

The collection software utilized with the PIV system was LaVision DaVis(Version 10.2.1). Each run captured a minimum of 500 image pairs (typically 1000 for redundancy), with delay between images of between 225-250 microseconds, as tabulated in Appendix II. The appropriate time delay (Δt) between the captured image pairs was calculated according to the anticipated maximum velocity ($U = 4$ m/s), the maximum desired displacement of the particles across images ($d_p = 12$ px), and the calculated pixel-to-mm ratio (r) as determined by calibration according to

$$\Delta t = \frac{d_p}{Ur} \qquad (1).$$

In general, the rule of thumb for estimating the appropriate time step is to ensure the highest expected velocity can be captured by PIV. Timing between laser pulses and camera imaging was achieved through the PTU with a response time of 10 ns and controlled by the Davis Software. The seeding density was approximately 10 particles per 12x12 pixel window.

3.4 Details of the Planar Evaluations

For each orientation considered (i.e. the x-y or y-z plane), multiple interrogation planes were chosen for evaluation. The planes of interest were chosen according to the zones where tensile coupons have been printed and evaluated in previous test campaigns to eventually facilitate corroboration of PIV data with tensile data [44]. The origin utilized in these orientations is at the lower left corner of the build plate, with Z = 0 mm being the build plate surface as shown in Figure 3.7. and as outlined previously in Figure 3.4a and 3.4b.

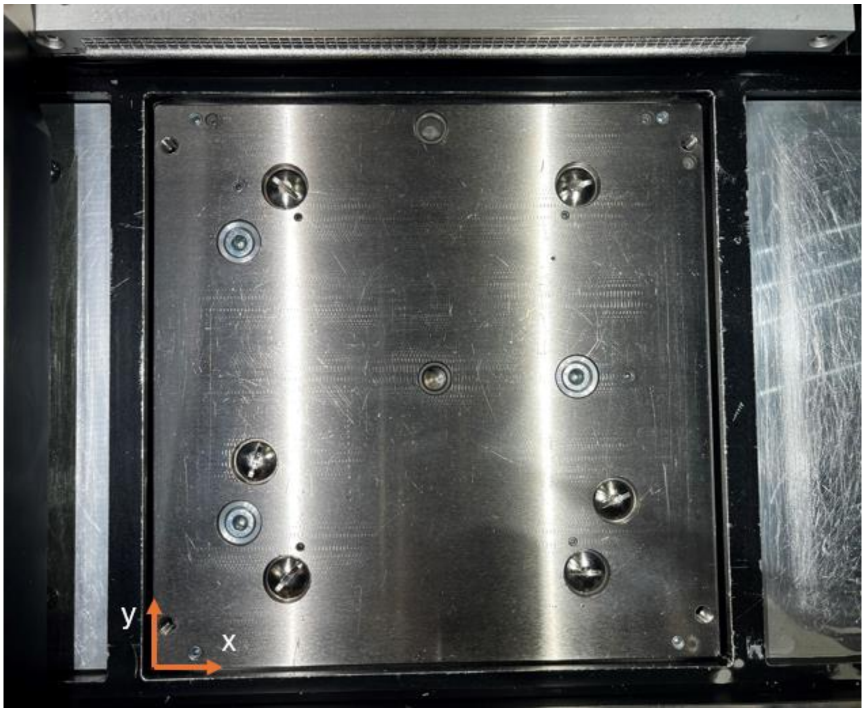

Figure 3.7: Location of origin for the XY Plots, with positive z oriented vertically from the build plate. Note the position of the lower grid nozzle in view.

There were two primary orientation planes that were explored in this investigation. The first plane of interest is designated the “YZ” plane, which is parallel to the laser path in the EOS M290 as shown in Figure 3.8. The second plane is designated the “XY” plane, which is perpendicular to the YZ plane and parallel to the build surface, and as shown in Figure 3.9.

The flow field in four different “YZ” planes were examined, which coincided with the center of the three build zones that are important in other research programs at the UW [44]. These three planes are oriented roughly 76 mm from each other. The middle plane (Plane 0, X = 125 mm) is centrally positioned across the width of the build plate and extends through the midsection of the build plate location as shown schematically in Figure 3.7b. Plane 12 (at X = 50 mm) intersects with the build zones 1 & 2. Similarly, Plane 34 (at X = 200 mm) intersects with build zones 3 & 4 of the UW Round Robin program as shown in Figure 3.7b. Finally, there is a plane that is near the left edge of the build plate at X = 3 mm, which is regarded as the “Dead Zone”. The Dead Zone was chosen for investigation due to powder dispersion being observed during builds and apparently because of divergent gas flow.

Akin to the YZ plane analysis, there were multiple XY planes of interest. These planes were defined with respect to their offset from the bottom of the mock-build chamber (i.e. the build plate), at distances of Z = 8 mm, Z = 13 mm, Z = 25 mm and Z = 35 mm. Each of the captured images for this orientation covered the entire build plate area.

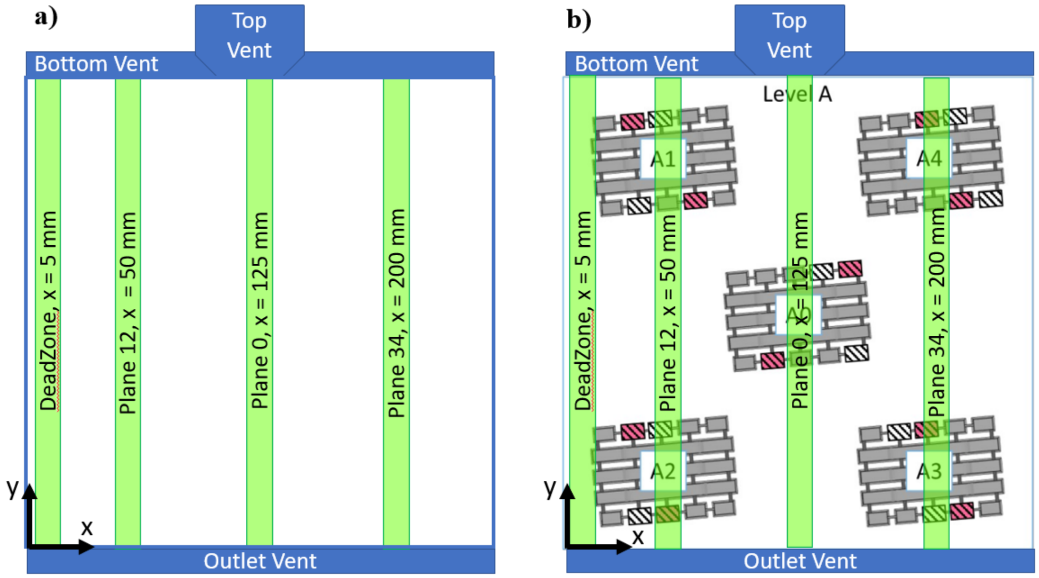

Figure 3.8: The YZ Planes as viewed from above the build plate, which is consistent with the EOS M290's incident laser axis (top view). a) the four planes of interest and their positions, b) YZ planes with build zone locations from UW Round Robin research overlaid [44].

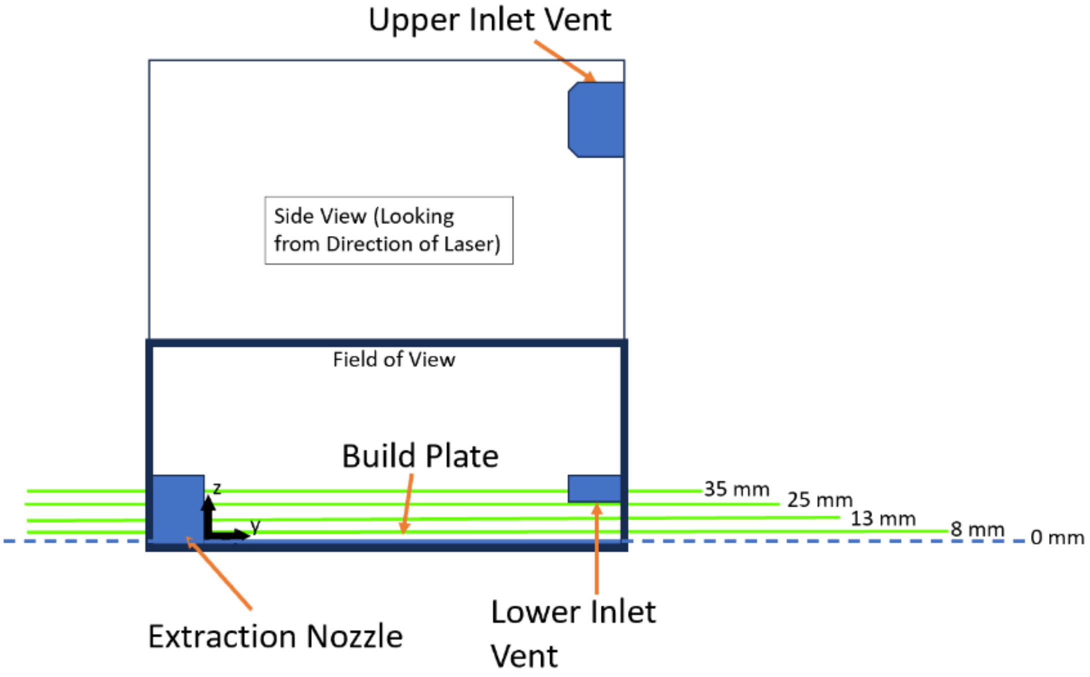

Figure 3.9: The XY planes of interest as viewed from the side of the mock build chamber, which is perpendicular to the x-axis.

3.5 Data Processing and Evaluation

Following data collection, LaVision DaVis was utilized to conduct cross-correlation of the captured data to create time-series flow fields. Geometric masking was applied when necessary, in conjunction with a background average subtraction algorithm, to reduce the effects of reflections and background noise. The window sizes selected for cross-correlation were adaptive, ranging from 156 px square to 32 px square to ensure adequate particle density. Window overlapping was set to be 75% Post-process visualization and plotting of the time-averaged flow-field data was conducted in Python utilizing a combination of packages including matplotlib, pandas, and seaborn.

A parameter commonly used in characterizing flow fields from PIV is the Turbulent Kinetic Energy (TKE), which quantifies the energy associated with eddies in the flow field. In three dimensions the TKE is generally calculated according to

$$k = \frac{1}{2}(R_{xx} + R_{yy} + R_{zz}) \tag{2}$$

where

$$R_{ij} = \overline{V_i V_j} = \frac{1}{N-1}\sum_{n=1}^{N}(V_{i,n} - \overline{V_i})(V_{j,n} - \overline{V_j}) \tag*{(3).}$$

The (R_{ij}) terms in Equation 3 correspond to the variance of velocity at a point ($V_{i,n}$) in relation to its time average ($\overline{V_i}$). For a two-dimensional case this can be simplified to the following planar expression:

$$k = \frac{1}{2}(R_{xx} + R_{yy}) \tag*{(4).}$$

Uncertainty Analysis

Methods for quantifying the quality of data have been developed for PIV. Some of these methods are incorporated in the LaVision software and others require error analysis to be performed utilizing Python scripts. Sciacchitano and Wieneke [46] provide an overview of uncertainty analysis and propagation in PIV. LaVision also provides detail on the background calculations conducted for uncertainty analysis in the flow field results [45]. Their methods are consistent with those of Sciacchitano & Wieneke. Each point in a flow field of interest will therefore be calculated with a time-based uncertainty. The primary uncertainty parameter in PIV is the uncertainty of a time-averaged velocity component, which is given by

$$U_{\bar{u}} = \frac{\sigma_u}{\sqrt{N}} \tag{5}$$

where σ_u and N are the standard deviation of the velocity, and the number of samples applied in the time-average respectively.

The uncertainty for vorticity is given by the following expression [46]:

$$U_\omega = \sqrt{2\left(\frac{1}{2d}\right)^2 [1 - \rho(2d)](U_u^2 + U_v^2)} \tag{6}$$

Similarly, the uncertainty for the Turbulent Kinetic Energy is given by:

$$U_{TKE} = \frac{1}{\sqrt{2N}}\sqrt{R_{uu}^2 + R_{vv}^2} \tag{7}$$

where d is the grid spacing, in meters, and ρ is the correlation value.

Chapter 4 RESULTS

4.1 XY Planes

Figure 4.1 shows the velocity distributions along the y-axis for the flow fields documented in the XY plane using PIV. Specifically, the velocity distribution is shown at offset distances from the build plate of Z = 8 mm, Z = 13 mm, Z = 25 mm, and Z = 35 mm in Figure 4.1a – 4.1d, respectively. There is a noticeable gradient in the velocity along the X-axis, which is most clearly evident near the inlet vent at Y = 175 mm. The gradient is most visible in the flow fields near the build plate that are shown in Figure 4.1a and 4.1b. In addition, the gradient was noted to have a periodic variation from left to right as it decayed. Lastly, the fields in Figure 4.1a and 4.1b show that the flow across the plate does not fully develop along the y-axis until approximately 50 mm from the nozzle.

Figure 4.2 shows the flow velocity along the y-axis for selected sections across the build plate with constant y. As evident in Figure 4.2 for Z = 13 mm, the maximum velocity is approximately 1.8 m/s in the upper left corner of the build plate (at X = 0 mm and Y = 175 mm). The velocity then decreases along the x-axis to less than 0.95 m/s at the right side of the build (Y = 250 mm), which represents a 47% decrease in velocity. It is important to note that the maximum velocity is located approximately 75 mm downstream from the inlet nozzle, which suggests there is a substantial component of out-of-plane flow (i.e. in the z-direction), which could cause entrainment or dispersion of powder from the build plate.

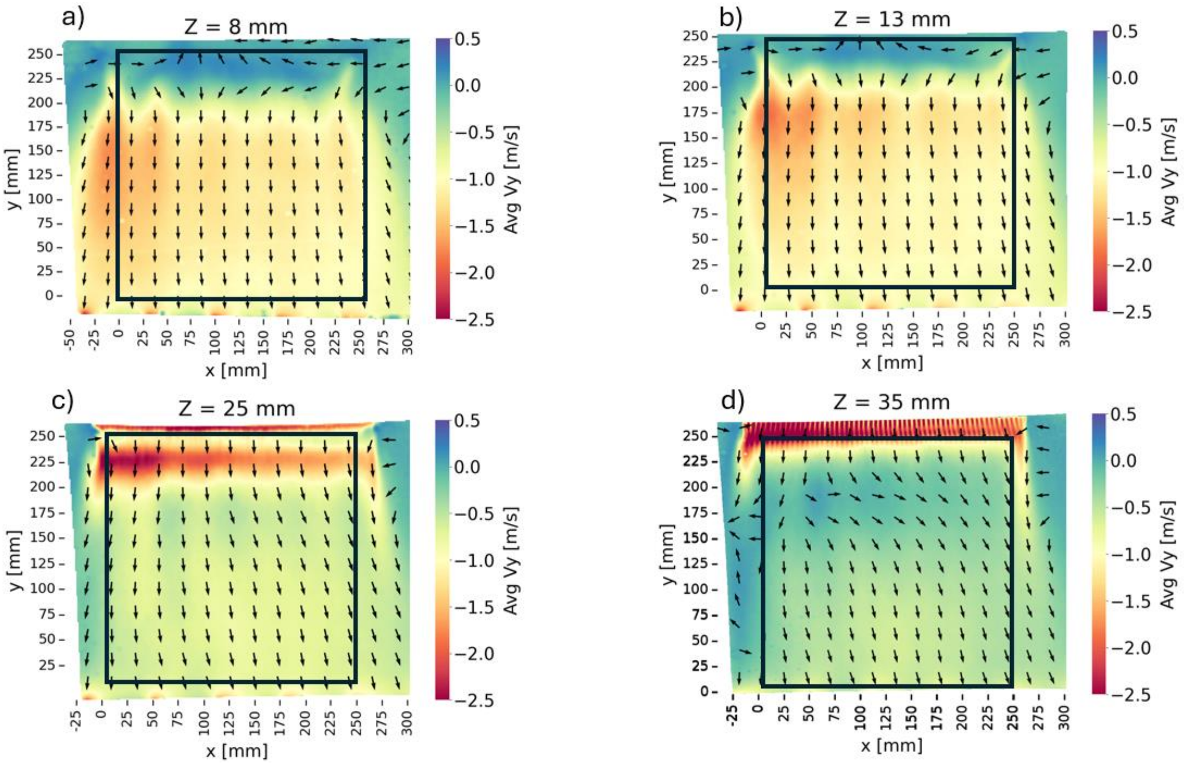

Figure 4.1: Gas flow velocity distribution along the y axis in the XY plane at varying distances from the build plate. a) Z = 8 mm, b) Z = 13 mm, c) Z = 25 mm, and d) Z = 35 mm offset from the build plate. Note the black square represents the position of the EOS M290 build plate, with the origin defined at the front left corner.

As the flow continues downstream, it is apparent that both the velocity and the gradient in velocity decrease. There is an exception to this behavior at Y = 250 mm, which is along the edge of the build plate and adjacent to the inlet, where the gas has not fully deflected from the inlet. This behavior is most evident at Z = 8 mm and Z = 13 mm in Figure 4.1a and Figure 4.1b, respectively.

Comparing the flow fields along the XY plane across these four cross sections reveals that the flow is not uniform or consistent among these four planes. In addition, there is an interesting behavior near the bottom inlet vent. The flow fields closest to the build plate, at Z = 8 mm and Z = 13 mm, show that there is an area directly downstream of the lower inlet that has very low gas flow velocity in the positive-y direction (close to 0 m/s). That behavior suggests that the cross-flow (the Y component of velocity) in that area isn't fully developed in these cross sections. For cross sections located farther from the build plate, e.g. at Z ≥ 25 mm, the velocity gradient along the x-axis is very clear, with maximum velocity of approximately 3 m/s at the left, and then decreasing to approximately 1 m/s at the right of the build plate, a reduction of 66%. Also of note, near the top of the lower inlet vent at Z = 35 mm in Figure 4.1d, there is a high velocity near the vent and then it diminishes rapidly as it proceeds along the y-axis.

An uncertainty analysis of the measured velocity was conducted with respect to time of at each point in the flow field as outlined in Chapter 3. Higher uncertainties would be expected in areas with greater variance in velocity. The average uncertainty for the data presented in Figure 4.2 was ± 0.0126 m/s, with individual values shown as error bands for each dataset.

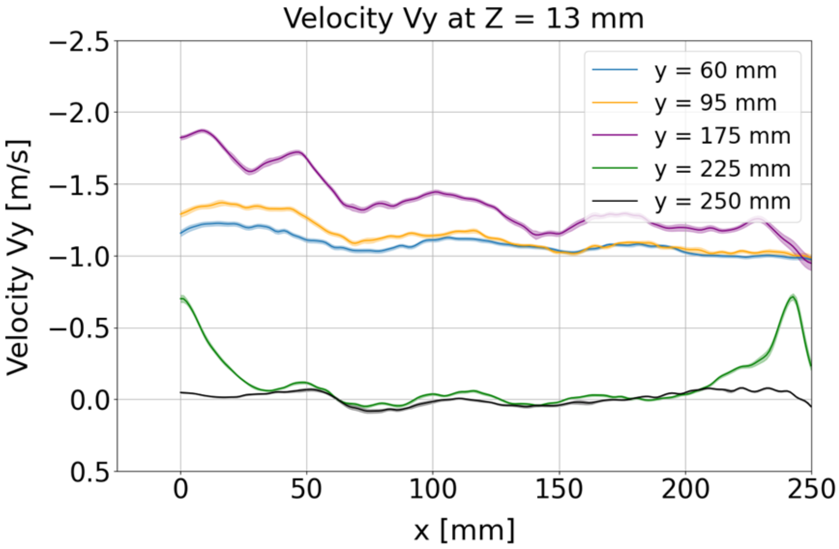

Figure 4.2: Velocity profiles within the XY plane located at Z = 13 mm from the build plate and described along the x-axis, i.e. across the entire build plate.

The vorticity of the XY flow distribution was also investigated to quantify the eddy generation and turbulence resulting from the rotational motion of the flow at each point in the flow field, with the goal of determining regions in the build plate that may lead to condensate becoming entrained. The time averaged instantaneous vorticity was calculated, and a moving average description of the vorticity within the XY planes was developed for lines of interest at Z = 8 mm as shown in Figure 4.3.At regions Y < 150 mm, the vorticity for each trajectory is roughly constant, however between Y = 150 and Y = 250 mm, the vorticity has some variation. In this region, the vorticity is highest at the edges of the build plate. . The uncertainty values for vorticity are higher compared to those for velocity because of the high spatial resolution of the dataset and 75% overlap, as outlined in the discussion provided by [46].

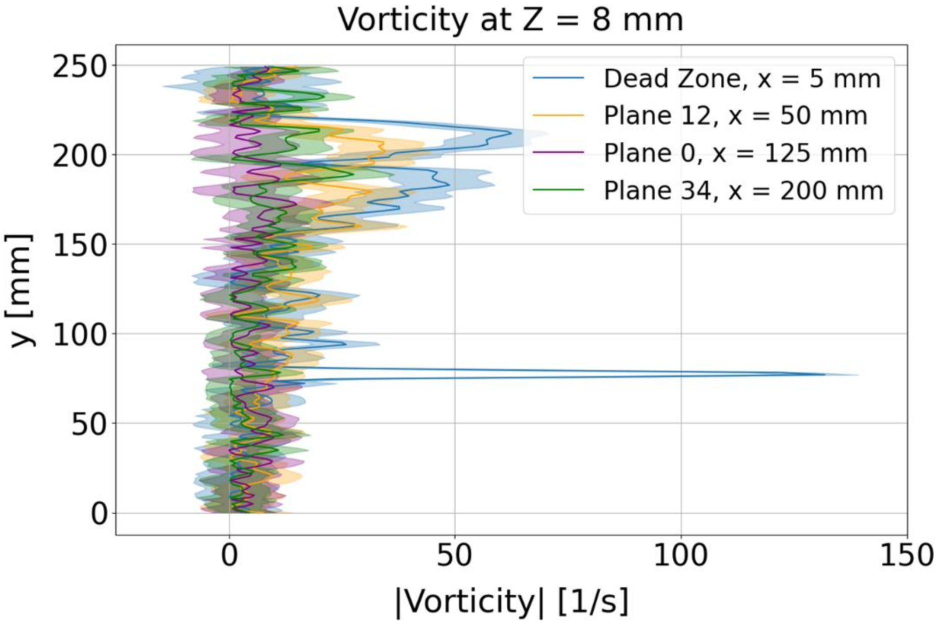

Figure 4.3: Vorticity distribution shown along y-axis at select x-slices and at Z = 8 mm from the build plate.

Measures of the turbulent kinetic energy (TKE) were also evaluated in the four planes of interest in the XY plane and are shown at various Z-offsets in Figure 4.4. The TKE is another commonly used representation of eddy strength, and may identify regions of the build plate that may entrain condensate. As evident in Figure 4.4a)-c), the maximum TKE is developed some distance downstream of the vent, corresponding to where the gas flow reaches its peak velocity. The TKE then decreases further downstream, indicating that the gas coming out of the lower inlet is highly turbulent due to its higher speed. An exception to these trends is show in Figure 4.4d), where the TKE is highest at Y = 250 mm. This trend is due to lower inlet flow being immediately deflected below Z = 35 mm, causing the relative TKE values to diminish in regions outside of the inlet jet.

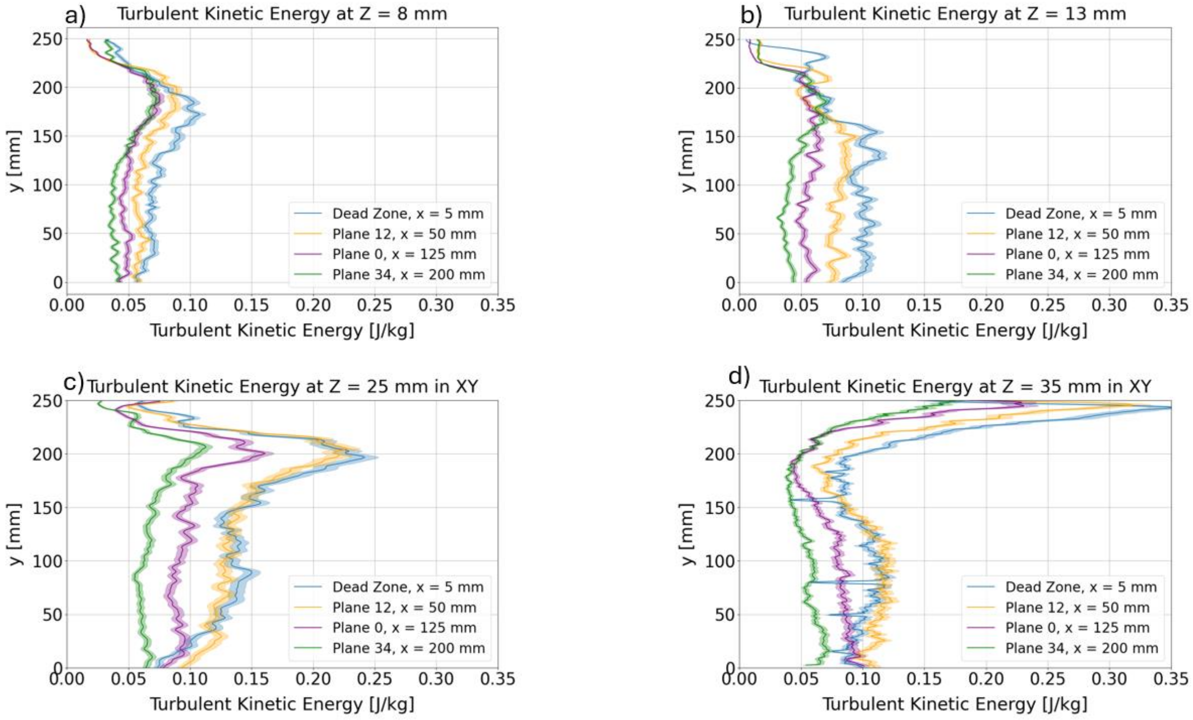

Figure 4.4: Turbulent kinetic energy distribution in the XY plane at a) Z = 8 mm, b) Z = 13 mm, c) Z = 25 mm, and d) Z = 35 mm.

4.2 YZ Planes

Velocity distributions for the flow fields in the YZ planes of interest are shown in Figure 4.5. The distributions shown in this figure represent the fields at four distinct distances along the x-axis, which intersect specific zones in the build plate. The cross section of the inlet flow for the various YZ planes all show similar patterns. The flow appears to reach a maximum at a Z height of approximately 25 mm to 30 mm from the build plate, which corresponds with the position of the lower inlet, and then diminishes (Figure 4.5) both above and below that level. The limited gas flow near the build plate and at the lower nozzle inlet, i.e., at Y = 250 mm as noted in Figure 4.1, is more clear in the YZ orientation. In addition, it is apparent that there is a vertical component of the flow in this region. In the region above the lower jet, the flow is being recirculated, which may lead to entrainment of condensate.

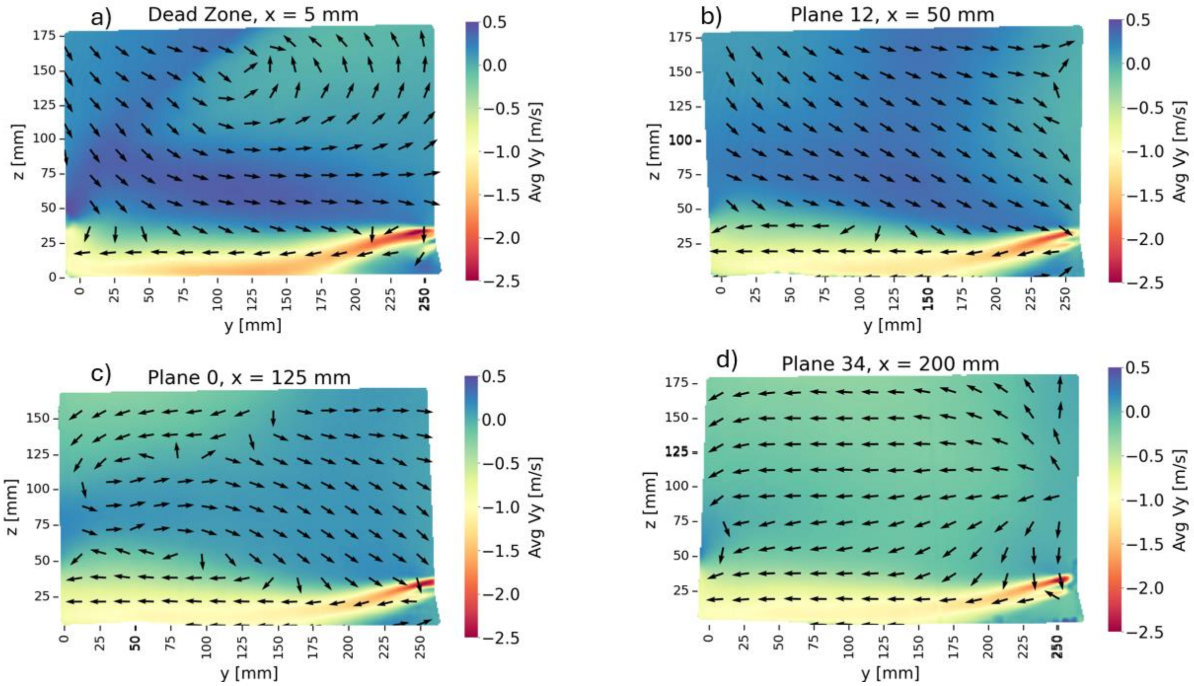

Figure 4.5: Gas flow velocity distribution along the y axis in the YZ plane at various distances across the build plate. a) Dead Zone, x = 5 mm, b) Plane 12, x = 50 mm, c) Plane 0, x = 125 mm, and d) Plane 34, x = 200 mm.

Similar to the evaluations performed on the velocity field within the XY planes of interest, the turbulent kinetic energy distribution was determined for the fields in the YZ planes. The TKE along the y-axis at Z =8 mm from the build plate is shown in Figure 4.6. The curvature evident in the TKE along the y-axis is in general agreement with that evident in the TKE plots shown for the XY planes. However, the magnitude in TKE is higher in the YZ distributions, suggesting that the eddies are stronger in that plane, as expected. The maximum TKE develops near the inlet vent and in the very left corner of the build plate, which is referred to here as the Dead Zone. In each plane of evaluation, the maximum value of the TKE is located between Y = 150 mm and 200 mm at Z = 8 mm.

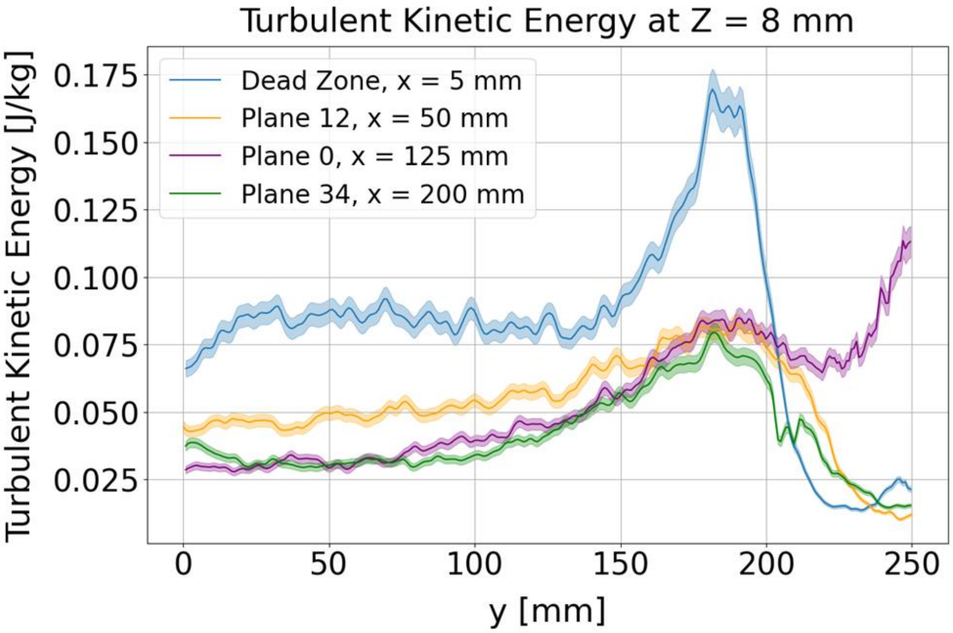

Figure 4.6: Turbulent kinetic energy for selected YZ Planes at an offset of Z = 8 mm from the build plate.

Figure 4.7 shows the turbulent kinetic energy for selected YZ planes at an offset from the build plate of 150 mm. As evident from these distributions, the TKE exhibits a very different profile than apparent in those closer to the build plate. Overall, the magnitude of the TKE is substantially lower than that corresponding to the flow inside the stream previously shown in Figure 4.6, potentially due this region being above the turbulent inlet jet. Furthermore, the deviation in turbulence at Z = 150 mm (Figure 4.7) is more pronounced than that for Z = 8 mm

(Figure 4.6). Within the Dead Zone there is a large gradient between Y = 50 mm and Y = 200 mm. Interestingly, the Dead Zone and Plane 0 show an initial decrease in TKE before a roughly linear increase is seen at Y = 200 mm. The distributions in Plane 12 and Plane 34 show the opposite trend. Unfortunately, it is not possible to compare these results to those for streamlines in the XY plane at Z = 150 mm to determine the out-of-plane eddy strength. Specifically, the velocity data for the XY planes was obtained within a range of 35 mm from the build plate.

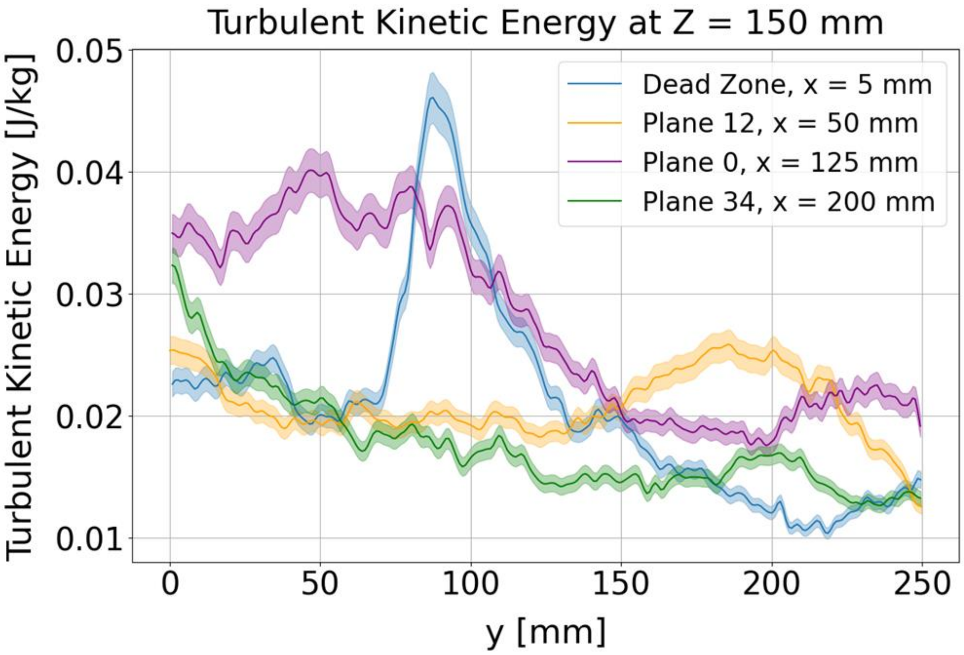

Figure 4.7: Turbulent kinetic energy for selected YZ Planes at an offset from the build plate of Z =150 mm. These distributions are valuable to compare with those in Figure 4.6, which were obtained much closer to the build plate.

Chapter 5 DISCUSSION

Results from the experimental evaluation using PIV showed that the gas flow distribution across the build plate and within the build envelope exhibited a substantial degree of spatial variation. While that is not unexpected, it is a concern if the variations in gas flow reduce its effectiveness in carrying the condensate to the exit baffle uniformly. Admittedly, this investigation is not the first to characterize gas flow within the build chamber of a commercial LPBF system. Therefore, a comparison of the findings with previous studies is warranted, in addition to a discussion to the aspects of the flow field that are most problematic and that should be corrected if possible.

5.1 Comparison with Literature

Weaver et al. [35] analyzed the gas flow in an EOS M290 utilizing hot wire anemometry (HWA) and discussed the limitations in fidelity of that approach. One observation that study that conflicts with results of the present study is a constant gas flow across the x-axis. In comparison, results from PIV testing presented here clearly showed that the flow distribution across the x-axis is not constant. The velocity gradients along the x-axis for different isolines extended along the y-axis are readily evident in Figure 4.2. A comparison of the gas flow velocity profile along the z axis (with coordinates of X = 125 mm and Y = 215 mm) between Weaver et al. and the present study is shown in Figure 5.1. The difference between these two profiles highlights one of the major benefits of PIV over HWA in this application, namely the fidelity in data is much finer for PIV. That refinement allows the localized velocity perturbations to be documented, which would have otherwise been missed by the coarser data collection of HWA.

Comparing the velocity profile results with those of Weaver et al. in Figure 5.1 at varying distances from the build plate reveals that the velocity documented from PIV is approximately 60% lower. One potential contribution to this discrepancy could be the differences in build cavity and gas medium measured; Weaver et al. conducted their experiments with an actual EOS M290, comparing measurements in nitrogen at 58 mbar between two nozzles, including the "standard" nozzle and the grid nozzle that is used in this study. Despite the discrepancy in the maximum velocity recorded, Weaver et al. does comment that the flow at the edge of the build plate near the inlet nozzle is not fully developed, which agrees with results of this investigation. Additionally, the PIV results show the peak velocity is at approximately Z = 20 mm, versus Weaver's results imply that it develops at Z = 10 mm. This could be due to the differences in the flow velocity and medium used, differences in the position of the build plate relative to the lower inlet between models, and differences in the fidelity of measurements; Weaver is interpolating from five data points.

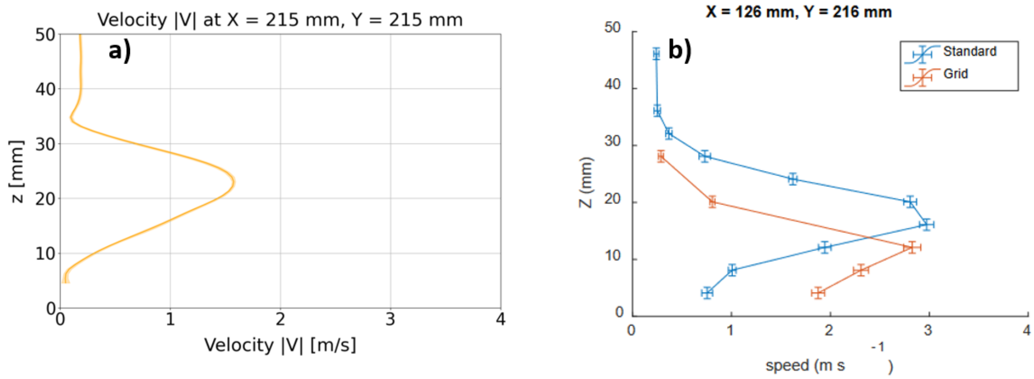

Figure 5.1: Comparison of gas velocity along the y-axis for Y = 215 mm as a function of distance from the build plate (z-axis) from a) PIV, and b) HWA from Weaver et. al [35]. Note in Weaver there was a comparison between a "Standard" Nozzle and "Grid Nozzle", the latter being the one in use in this study. Additionally, the process parameters, such as operating gas and differential pressure settings used by Weaver et al. are different from those approximated in the PIV study.

Figure 5.2 provides a comparison between results of Elkins et al. [41] with those of the present investigation. As described in Chapter 2, Elkins evaluated the gas flow along the y-axis within a 1/3rd scale model of an EOS M290 build chamber utilizing Magnetic Resonance Velocimetry (MRV). These results correspond to the measurements obtained from PIV for an XY plane located at $Z = 8$ mm offset from the build plate. As evident from this comparison, the overall profile from Elkins in Figure 5.2a is more symmetric along the x-centerline of the build plate and lacks the velocity gradient apparent in Figure 5.2b that was revealed by PIV. Also apparent from the overlaid build plate (bold square outline) in the work of Elkins et al., the top edge of the build plate does not receive sufficient cross flow, which is consistent with the results presented in Section 4.1. Hence, based on results from MRV and PIV in Figure 5.2, both experimental approaches show that the inert gas cross flow does not fully cover the build plate. Interestingly, the results from Elkins in Figure 5.2a shows the flow field reaching the build plate at approximately the same Y position as the PIV results at $Z = 8$ mm, even though the plane of interrogation is 7.5 mm lower. Further work in testing interrogation planes closer to the build plate ($Z < 8$ mm) would be useful in verifying Elkins' results.

The discrepancy in results between these two approaches regarding the velocity gradient could be due to variations in the experimental setup. Most notable, the fluid mediums were different as Elkins used water versus air. However, the Reynolds Numbers are close enough in the two studies ($Re=36000$ for Elkins, $Re = 39000$ for PIV) to expect similitude. The data of Elkin et al. [41] does show a symmetric distribution that resembles a turbulent vent flow profile that could be established in a duct without vanes. Alternatively, it suggests a reduced effect of the vent vanes in the Y-Duct in their experiment. However, it is unknown if their Y-Duct incorporated vanes as these details were not reported.

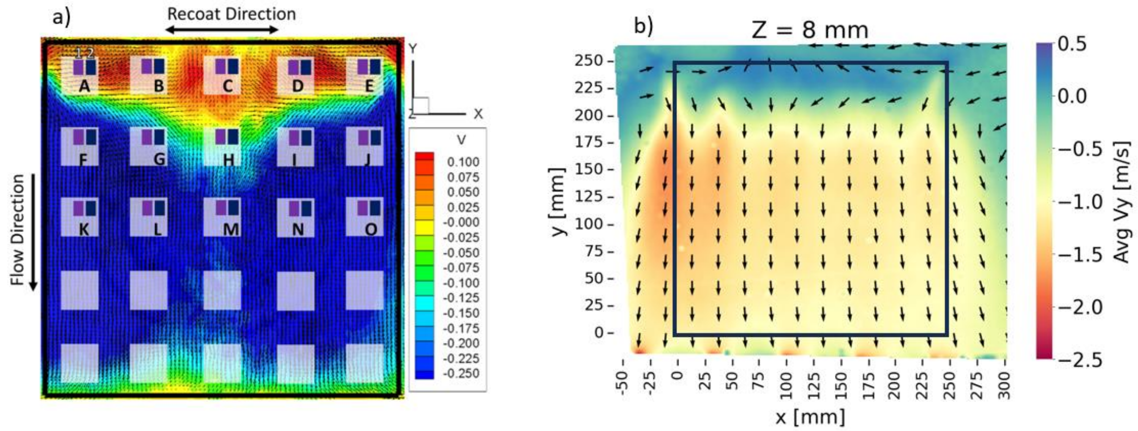

Figure 5.2: A comparison of the flow field at the build plate obtained from a) MRV experiments (Z = 0.5 mm) performed by Elkins et. al [41] with b) results obtained from PIV data in the present investigation obtained at Z = 8 mm. Note the symmetry in the field from Elkins et al. with the asymmetric distribution obtained using PIV.

5.2 Velocity Variability from Vent Curvature

A velocity gradient was apparent across the build plate in the XY plane views of the velocity distribution. The planes with offsets of Z = 8 mm and Z =13 mm from the build plate exhibited the largest gradient (Figure 4.1) and which appeared to reach the build plate at approximately 175 mm from the build plate origin, i.e. roughly 75 mm from the gas inlet. The source of this gradient could potentially be attributed to the curvature in the Y-Duct design, which is also compounded by the variable cross section in both surface area and general shape. As the entrance flow reaches the bend in the Y-Duct, the estimations for Reynolds Number are well within the turbulent regime (Re > 2500). Since the Y-Duct has a rectangular cross section at the exit, a hydraulic diameter calculation should be used to estimate the Reynolds number, which is estimated to be approximately 14,000 at the exit (excluding the vanes). However, due to the split circular geometry seen in the Y-Duct, the Reynolds number at the entrance would be different. The inlet speed upstream of the Y-Duct was calculated from the differential pressure gauge as 7.2 m/s. That results in an estimated Reynolds number at the entrance of Re = 42,000. Therefore, the flow can be assumed to be turbulent, leading to a cumbersome fluids problem to numerically model.

In conjunction with the addition of straightening vanes, the curvature of the Y-Duct could also cause the velocity gradient seen in Figure 4.2. If each vane is approximated as a single pipe, the outer vanes will be longer than the inner vanes as evident in Figure 5.3. Rough measurements of the vane length indicate that inner and outer vanes have a path length difference of approximately 250 mm, corresponding to lengths of 127 mm and 380 mm, respectively. As such, the effect of skin friction drag would reduce the velocity in the outer vents more than the inner vents, promoting a gradient in velocity akin to that observed in Figure 4.2.

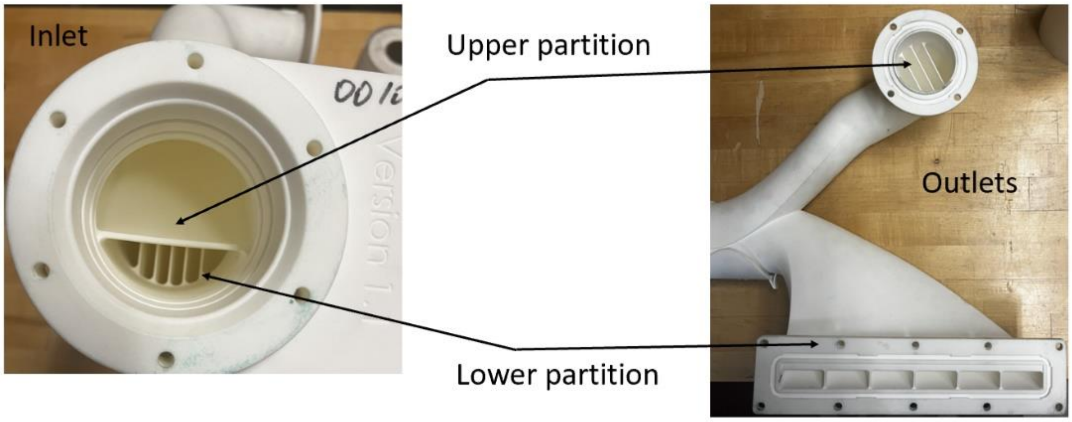

Figure 5.3: Lower inlet and outlets of the y duct. Note for the lower partition, the length at the left (inside of curve) is shorter than to the right (outside of curve), and the presence of straightening vanes throughout the path length.

5.3 Variability in Vent Velocity

The other major characteristic of note in the velocity profiles presented in Figure 4.2 was the periodic behavior, which is also apparent to some extent in Figure 4.1. A potential cause to this fluctuation in the flow is the positions of the internal vanes present in the Y-Duct that are apparent in Figure 5.3. These vanes extend through the curvature of the lower vent, and allegedly are there to serve as flow straighteners to ensure the gas propagates along the y-axis of the build chamber after exiting the vent. However, it is possible that the vanes induce a viscous flow effect akin to that in pipes, where the flow profile across the cross-section is roughly parabolic due to a no-slip condition at the walls. Therefore, the distribution in Figure 4.2 may arise from the periodic no-slip condition serving as the low point, and then the peaks being representative of the free-stream. To the author's knowledge, this investigation is the first to report this characteristic in the velocity distribution in the gas flow of the EOS M290. Although a uniform flow field would be most desirable, this fluctuation resulting from the vanes is not necessarily detrimental. Nevertheless, it could be useful in future work to evaluate the flow in a ducting system without the vanes if the opportunity arises.

5.4 Velocity Profile Variation

As seen in the YZ Views of the flow distribution in Figure 4.5, there is an interesting trend in the velocity profiles at the lower vent. Specifically, it appears that the gas flow does not immediately reach the build surface. In addition, the flow has much lower velocity above and below the vent than the flow exiting from the vent. It would appear most beneficial for the flow to reach the build surface and as soon as possible to ensure that the coverage of the back of the build plate is uniform. Results from PIV show that the leading edge of the build plate does not receive adequate flow coverage. The lower inlet design has two sections, including a primary upper section with principal vane direction oriented along the y-axis and a lower section having a more aggressive downward angle to direct flow air towards the build plate. The lower inlet design is shown in Figure 5.4a and the bottom row of vents that are intended to deflect a portion of the flow downwards is shown in Figure 5.4b. Hence, the intended flow is formed by two portions of the lower vent. However, according to the results obtained using PIV, the lower section does not seem to perform its intended duty. In essence, the nozzle does not adequately push the gas downwards to ensure that the entire build plate experiences adequate crossflow at the surface. This is an aspect of the flow field that could be corrected with an improved nozzle design. In addition, further evaluation of this aspect of the flow distribution could be improved by either performing complementary XZ planar evaluations of the flow near the back wall or using stereo PIV. Those activities could have additional value in further evaluation of the Dead Zone and reduction of its severity.

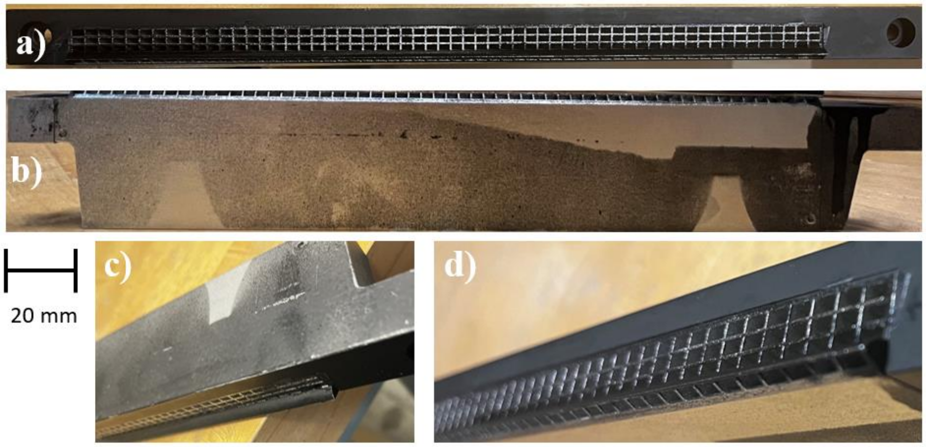

Figure 5.4: Close-up view of the lower vent. a) Front view, viewing the vent grating, b) bottom view, with deflection grating facing the viewer, c) oblique view of top of grating, and d) oblique view of bottom of grating.

5.5 Vorticity & Turbulent Kinetic Energy

The vorticity and TKE flow parameters are important measures that were adopted to assess the quality of the flow field. Vorticity provides a representation of the recirculation of the flow in different regions. Turbulent Kinetic Energy provides a quantitative representation of the variation in the flow field over time, which provides a potential measurement of the effectiveness of the gas flow in removing laser-powder interaction byproducts. In their application here, they reflect the potential for condensate entrainment or redeposition due to inhomogeneous gas flow, which is expected to increase with either the TKE or vorticity. These are common root causes for defects as described by Ladewig et al. [3].

There was a variation in the flow vorticity examined along the y axis that is evident in Figure 4.3, which could be attributed to turbulence in the gas flow. It can be inferred from the flow distributions in the YZ plane that the gas flow is turbulent near the inlets, which could promote more swirling of condensate at the rear edge of the build plate. However, near the center of the field, the time averaged vorticity is lower, indicating that the flow is more uniform near the center of the build plate. The vorticity increases near the outlet as well, which suggests that the flow may be stagnating at the exit baffle, potentially due to its geometry.

It is important to note that the turbulent kinetic energy and vorticity plots are calculated differently in the YZ and XY planes. For the YZ plane, the velocity components used in the calculation of TKE are derived from the Y and Z components of velocity; the vorticity is calculated from their cross-derivatives. In the XY plane, the velocity components are obtained from the X and Y components of velocities.

The TKE is higher for the YZ plane than in for the XY plane, suggesting that there is greater turbulence in the YZ plane due to eddies that are formed. In comparison, the velocity components of these eddies in the XY plane are not as strong. The implication of having stronger eddies in the YZ plane is that it could cause greater redeposition of condensate onto the build surface due to entrainment of the condensate within the vortex. Condensate may also accumulate above the lower inlet jet and attenuate the incident laser, which reduces the effective power prior to reaching the powder bed. As outlined in Section 2.2, an increase in condensate is expected to reduce part quality and performance due to the many potential contributions of condensate in defect generation.

The TKE was shown to be greater near the left of the build plate for both YZ and XY analysis planes (Figure 4.4 & Figure 4.6). That region is closest to the recoater home position and the left wall. The pressure boundary condition caused by the recoater and wall may cause an increase in eddy formation. When looking at TKE in the jet in the YZ plane, the TKE was much higher near the left wall (Dead Zone) than it was at any other position, which warrants further evaluation.

In Figure 4.7, the TKE has more variation above the lower jet as viewed across the evaluated planes. That behavior suggests that condensate that rises above the lower jet could become suspended in the region between the upper and lower vent jets. As described earlier, entrained condensate could absorb some of the laser energy before it reaches the powder bed, thereby contributing to power attenuation and the generation of lack-of-fusion defects.

Although there is a possibility that the detrimental aspects of the flow field could be corrected by increasing the inlet velocity of the inert gas, that seems unlikely and may introduce issues associated with powder pickup. An alternate and more favorable approach to improving the flow field is to redesign the ducting and the inlet vents to overcome the drawbacks identified. The key components of the flow field that need correction are i) the delayed development of cross-flow from the lower inlet, ii) the undesirable aspects of the flow field in the dead zone, iii) the high vorticity in the center of the build chamber that could entrain condensate and that interferes with the incident laser, as well as iv) the gradient in the flow from the left to the right of the build plate. Future work should be directed in this area.

5.6 Limitations

Results from this investigation provide new understanding of the inert gas flow distribution within the build chamber of the EOS M290, a commercial machine for LPBF. Overall, there were several undesirable characteristics of the gas flow and regions of concern that were identified. Potential contributions from the ducting and nozzles to these aspects of the flow were described, as well as suggestions for correcting these problems or the need for future work were discussed. Despite the value of these findings, there were limitations to the investigation that are important to highlight. To start, air was utilized as the working medium instead of argon, which has differences in density and viscosity. The flow was matched to Reynolds Number, which is an approximation commonly used in fluid mechanics studies to justify the replacement of argon with air. But there could be other differences that are not recognized, such as temperature and differences in the ducting upstream of the y-duct between the MBC and the EOS M290. Additionally, the EOS M290 utilizes filters in the gas system to remove condensate from the argon prior to it being recirculated back into the system. These filters become saturated with use, and cause blockage of the flow. The feed turbine compensates by running at a higher RPM to maintain the volume flow rate, however this may result in variations in the inlet flow profile or the partition of flow at the y-duct.

Another important consideration is that the experimental evaluations only provide information along two-dimensional slices of the build volume, and information regarding out-of-plane velocities was not documented. If these out-of-plane velocities are of high enough magnitude, errors could be introduced in the flow fields documented in this investigation. One aspect of the flow field that was not examined was the flow within the XZ plane. Evaluation of the flow in the back of the machine within the XZ plane could provide a better understanding of the function of the lower inlet nozzle and the contributing factors to the dead zone. Other differences worthwhile to consider between the flow field in an EOS M290 and from the apparatus discussed could be related to temperature of the build volume, rake position, and the effects of the EOS M290's filtration system. Nevertheless, the results obtained in this investigation have provided a foundation of knowledge that can serve to support future efforts focused on further understanding gas flow in the EOS M290 and other LPBF systems.

Chapter 6 CONCLUSIONS AND FUTURE WORK

6.1 Conclusions

Particle Image Velocimetry (PIV) was adopted to evaluate the inert gas flow distribution within a mock build chamber of the EOS M290 laser powder fusion system. The mock build chamber consisted of a 1:1 scale model, developed through collaboration with Boeing engineers, that utilized original equipment for the upper and lower inlet nozzle and Y-Duct. Results of the gas flow distribution were documented in two orthogonal planer views, that enabled visualization of the flow across the build chamber (XY plane) and over the build envelope from the front to the back of the machine (YZ plane). Results showed that there are spatial variations in the gas flow within both planes, which may be detrimental to the quality of metal produced and consequent spatial variations in printing defects and mechanical properties of component parts. With the combined results from the YZ and XY Planes, a three-dimensional experimental approach may be redundant. In evaluation of the flow field in the XY plane, a noticeable gradient in velocity was evident along the x-axis, that was most apparent near the build surface. In addition, a periodic behavior was evident in the velocity distribution across the build plate. Both flow characteristics could be due to the design of the Y-Duct and lower inlet nozzle. Regarding the Y-Duct, the undesirable aspects of the flow appear to be attributed specifically to two design factors, including the curvature and internal vane geometry. The current Y-Duct design appears to cause the velocity gradient, reflected as slower flow on the right-side of the build plate, due to the different path lengths of air traveling on the inside and outside aspects of the curved duct design. The sinusoid behavior appears to be due to the vanes inducing a no-slip condition at their walls, which would cause a lower velocity in these regions compared to the free-stream regions.

These characteristics of the gas flow could be improved or overcome by new duct and nozzle designs.

6.2 Future Work

Further investigation of the flow field resulting from the current vent geometry and that results from modifications of the nozzle should be performed to obtain a better understanding of the flow field in the build space. One aspect of the flow field that was not evaluated using PIV was that in the XZ plane. The vertical component of the gas flow across the back of the build plate would be valuable to understand and would provide information on if there is recirculation in the XY plane in areas above the lower jet. Verification of the flow field at the lower inlet could be conducted by utilizing a pitot rake. Further analysis of the correlation between flow characteristics and metal microstructure and properties should also be performed. Specifically, the microstructure and mechanical properties of metal produced in locations of the build plate should be correlated with the gas flow characteristics. That could provide insights on the localized effect of gas flow on part performance. Further improvements to the Mock Build Chamber design could be to more directly match the ducting system upstream of the Y-duct, and to model the effects of filter saturation on gas flow. Additional research concerning the effect of modifications in vent design and on the gas delivery system should be performed using PIV.

Appendix I. PIV System Specifications

Equipment	**Specifications**
Imager sCMOS Camera	5.5 Megapixel
Camera Accessories	50 mm and 60 mm Nikon lenses, LaVision Scheimpflug,adapter (1108176), Manfrotto tripod
Evergreen 200 Laser w/ Power Supply	200 mJ laser @ 532 nm. Double-pulsed
Optical Equipment for Laser	Enclosed 90° mirror and f = -10 mm divergent lens
Programmable Timing Unit	PTU-X
PC w/ LaVision Software	LaVision DaVis 10.2
Calibration Plate	3D, # 204-15

Appendix II. Image Timing

Experiment Name	**Delay (µs)**
XY Z = 8 mm	225
XY Z = 13 mm	232
XY: Z = 25 mm	232
XY: Z = 35 mm	232
YZ: Dead Zone	250
YZ: Plane 12	240
YZ: Plane 0	250
YZ: Plane 34	250

Appendix III. PIV Processing Specifications

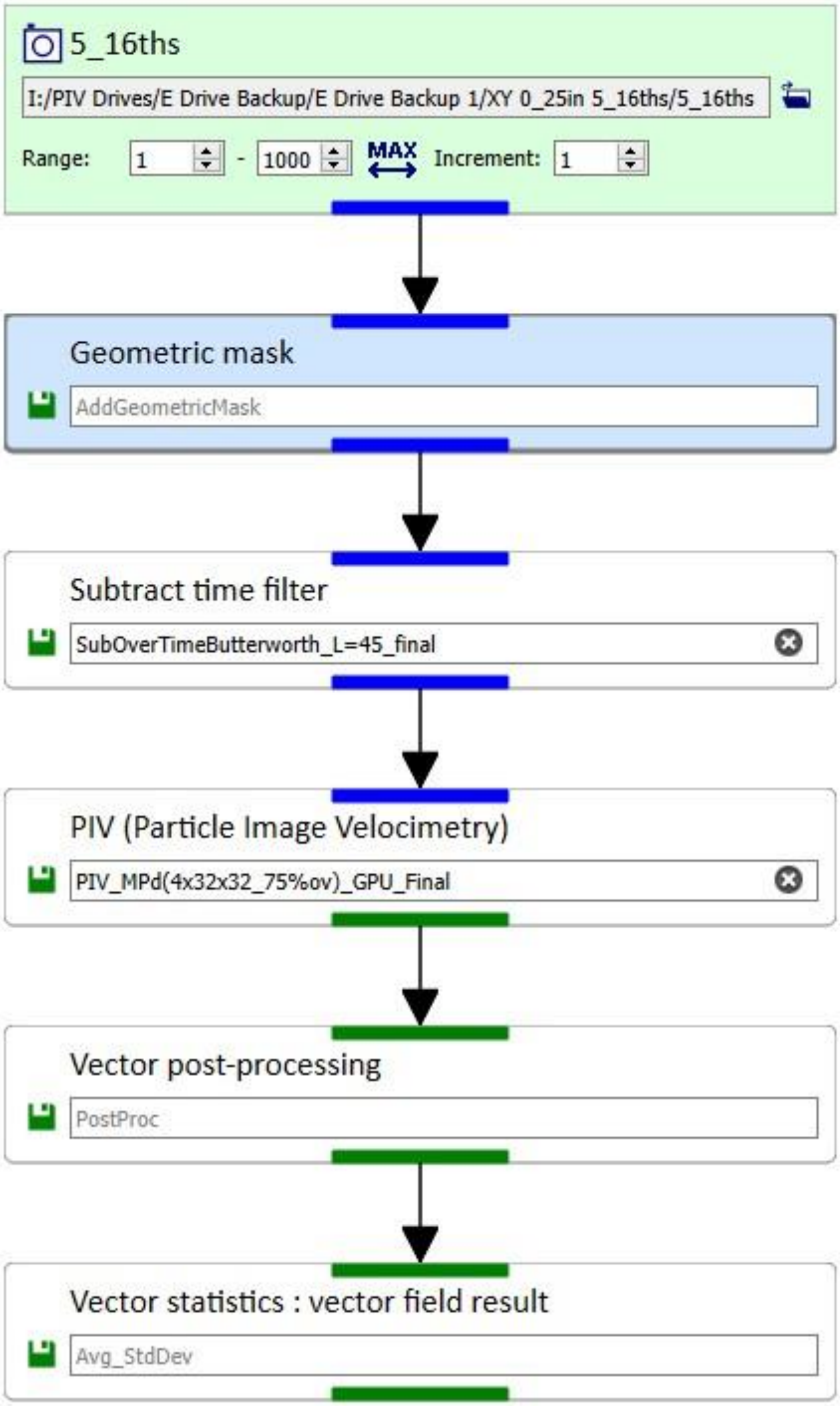

5_16ths

I:/PIV Drives/E Drive Backup/E Drive Backup 1/XY 0_25in 5_16ths/5_16ths

Range: 1 - 1000 MAX Increment: 1

Geometric mask

AddGeometricMask

Subtract time filter

SubOverTimeButterworth_L=45_final

PIV (Particle Image Velocimetry)

PIV_MPd(4x32x32_75%ov)_GPU_Final

Vector post-processing

PostProc

Vector statistics : vector field result

Avg_StdDev

Figure III.1: LaVision PIV Processing Tree

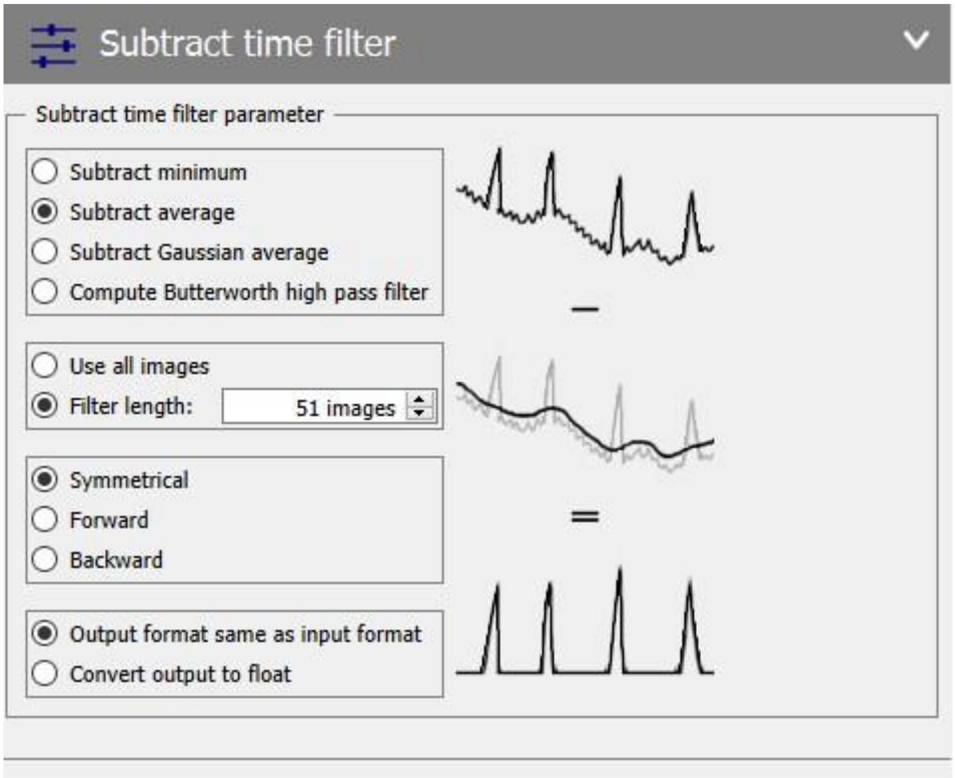

Subtract time filter

Subtract time filter parameter

○ Subtract minimum
● Subtract average
○ Subtract Gaussian average
○ Compute Butterworth high pass filter

○ Use all images
● Filter length: 51 images

● Symmetrical
○ Forward
○ Backward

● Output format same as input format
○ Convert output to float

Figure III.2: Subtractive Filter Settings.

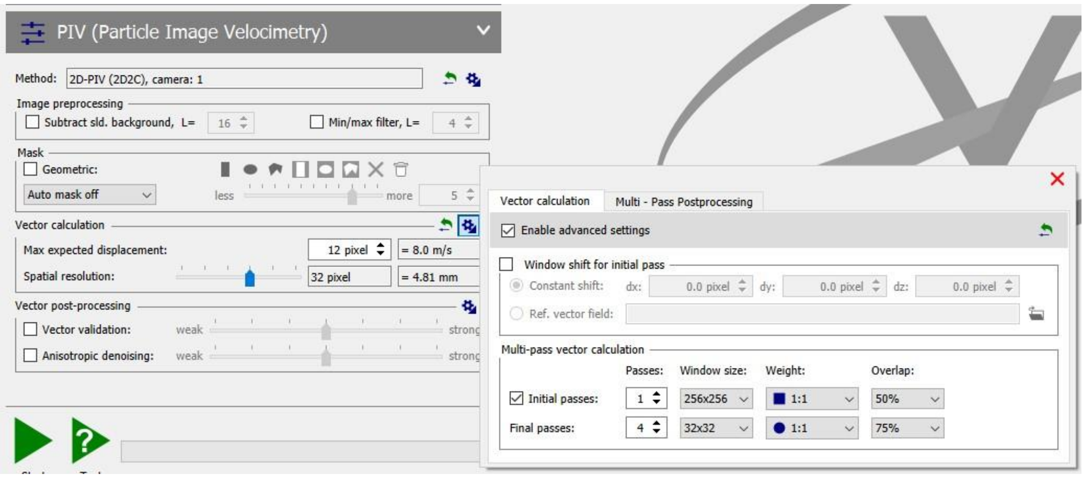

PIV (Particle Image Velocimetry)

Method: 2D-PIV (2D2C), camera: 1

Image preprocessing
☐ Subtract sld. background, L= 16
☐ Min/max filter, L= 4

Mask
☐ Geometric:
Auto mask off
less more 5

Vector calculation
Max expected displacement: 12 pixel = 8.0 m/s
Spatial resolution: 32 pixel = 4.81 mm

Vector post-processing
☐ Vector validation: weak strong
☐ Anisotropic denoising: weak strong

Vector calculation | Multi - Pass Postprocessing

☑ Enable advanced settings

☐ Window shift for initial pass
○ Constant shift: dx: 0.0 pixel dy: 0.0 pixel dz: 0.0 pixel
○ Ref. vector field:

Multi-pass vector calculation

	Passes:	Window size:	Weight:	Overlap:
☑ Initial passes:	1	256x256	■ 1:1	50%
Final passes:	4	32x32	● 1:1	75%

Figure III.3: PIV Multipass settings

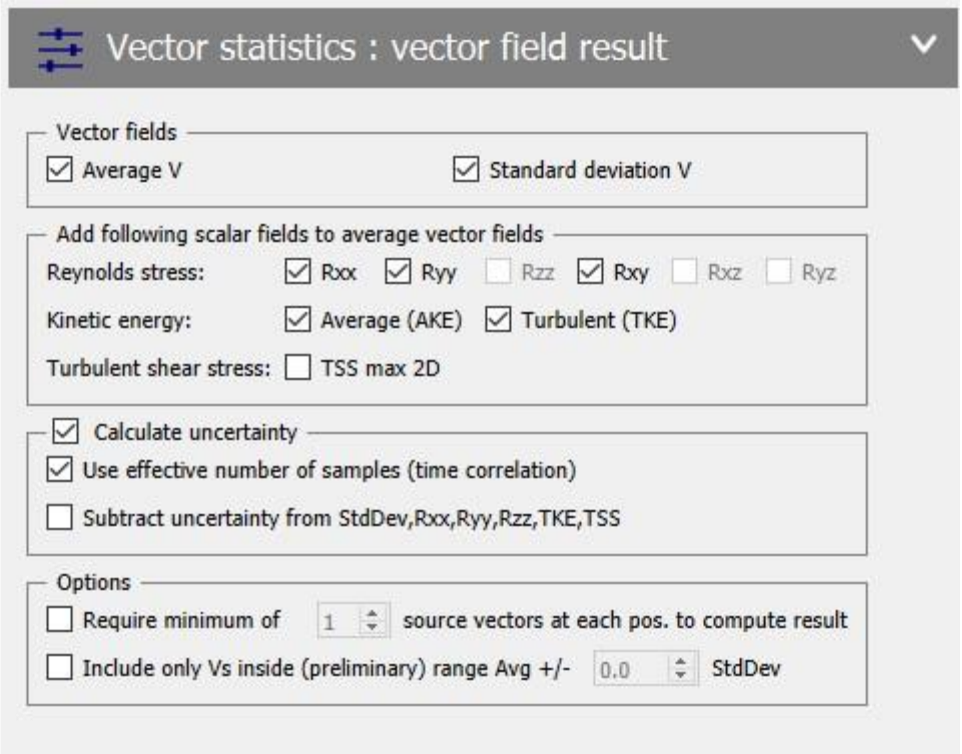

Vector statistics : vector field result

Vector fields

☑ Average V ☑ Standard deviation V

Add following scalar fields to average vector fields

Reynolds stress: ☑ Rxx ☑ Ryy ☐ Rzz ☑ Rxy ☐ Rxz ☐ Ryz

Kinetic energy: ☑ Average (AKE) ☑ Turbulent (TKE)

Turbulent shear stress: ☐ TSS max 2D

☑ Calculate uncertainty

☑ Use effective number of samples (time correlation)

☐ Subtract uncertainty from StdDev,Rxx,Ryy,Rzz,TKE,TSS

Options

☐ Require minimum of 1 source vectors at each pos. to compute result

☐ Include only Vs inside (preliminary) range Avg +/- 0.0 StdDev

Figure III.4: Vector Field Visualization Settings.

WORKS CITED

[1] A. Gaikwad, R. J. Williams, H. de Winton, B. D. Bevans, Z. Smoqi, P. Rao and P. A. Hooper, "Multi phenomena melt pool sensor data fusion for enhanced process monitoring of laser powder bed fusion additive manufacturing," *Materials & Design,* no. 221, pp. 110919-110941, 2022.

[2] Z. A. Young, Q. Guo, N. D. Parab, C. Zhao, M. Qu, L. I. Escano, K. Fezzaa, W. Everhart, T. Sun and L. Chen, "Types of spatter and their features and formation mechanisms in laser powder bed fusion additive manufacturing process," *Additive Manufacturing,* vol. 36, p. 101438, 2020.

[3] A. Ladewig and G. Schlick, "Influence of the shielding gas flow on the removal of process by-products in the selective laser melting process," *Additive Manufacturing,* vol. 10, pp. 1-9, 2016.

[4] P. Bidare, I. Bitharas, R. M. Ward, M. M. Attallah and A. J. Moore, "Laser Powder Bed Fusion in High-Pressure Atmospheres," *The International Journal of Advanced Manufacturing Technology,* vol. 99, pp. 543-555, 2018.

[5] J. Reijonen, A. Revuelta, T. Riipinen, K. Ruusuvuori and P. Puukko, "On the effect of shielding gas flow on porosity and melt pool geometry in laser powder bed fusion additive manufacturing," *Additive Manfuacturing,* vol. 32, p. 101030, 2020.

[6] A. M. Philo, C. J. Sutcliffe, S. Sillars, J. Sienz, S. G. Brown and N. P. Lavery, "A study into the effects of gas flow inlet design of the Renishaw AM250 laser powder bed fusion machine using computational modeling," in *Solid Freeform Fabrication Symposium*, Austin, TX, 2017.

[7] H. Carson, B. Allen, B. Vu, G. Howard and N. Lee, "Final Project Report: Boeing AM Powder Bed Fusion Part Porosity Sources," University of Washington, Seattle, WA, 2022.

[8] S. Cooke, K. Ahmadi, S. Willerth and R. Herring, "Metal additive manufacturing: Technology, metallurgy and modelling," *Journal of Manufacturing Processes,* vol. 57, pp. 978-1003, 2020.

[9] B. Blakey-Milner, P. Gradl, G. Snedden, M. Brooks, J. Pitot, E. Lopez, M. Leary, F. Berto and A. du Plessis, "Metal additive manufacturing in aerospace: A review," *Materials & Design,* vol. 209, p. 110008, 2021.

[10] F. Trevisan, F. Calignano, A. Aversa, G. Marchese, M. Lombardi, S. Biamino, D. Ugues and D. Manfredi, "Additive Manufacturing of titanium alloys in the biomedical field: processes, properties and applications," *Journal of Applied Biomaterials & Functional Materials,* vol. 16, no. 2, pp. 57-67, 2018.

[11] L. Dowling, J. Kennedy, S. O'Shaugnessy and D. Trimble, "A Review of Critical Repeatability and Reproducibility Issues in Powder Bed Fusion," *Materials and Design,* vol. 186, p. 108346, 2020.

[12] E. Santecchia, S. Spigarelli and M. Cabibbo, "Material Reuse in Laser Powder Bed Fusion: Side Effect of the Laser - Metal Powder Interaction," *Metals,* vol. 10, p. 341, 2020.

[13] N. Read, W. Wang, K. Essa and M. M. Attallah, "Selective laser melting of AlSi10Mg alloy: Process optimization and mechanical properties development," *Materials and Design,* vol. 65, pp. 417-424, 2015.

[14] Z. Chen, X. Wu and C. H. Davies, "Process variation in Laser Powder Bed Fusion of Ti-6Al-4V," *Additive Manufacturing,* vol. 41, p. 101987, 2021.

[15] C. U. Brown, G. Jacob, M. Staudt, S. Moylan, J. Slotwinski and A. Donmez, "Interlaboratory Study for Nickel Alloy 625 Made by Laser Powder Bed Fusion to Quantify Mechanical Property Variability," *Journal of Materials Engineering and Performance,* vol. 25, no. 8, pp. 3390-3397, 2016.

[16] D. Riabov, L. Cordova, E. Hryha and S. Bengtsson, "Effect of Powder Variability on Laser Powder Bed Fusion Procesing and Properties of 316L," *European Journal of Metals,* vol. 2, no. 1, pp. 202-221, 2022.

[17] J. Reijonen, R. Bjorkstrand, T. Riipinen, Z. Que, S. Metsa-Kortelainen and M. Salmi, "Cross-Testing Laser Powder Bed Fusion Production Machines and Powders: Variability in Mechanical Properties of Heat-Treated 316L Stainless Steel," *Materials & Design,* vol. 204, p. 109684, 2021.

[18] P. Edwards and M. Ramulu, "Fatigue performance evaluation of selective laser melted Ti-6Al-4V," *Materials Science & Engineering A,* vol. 598, pp. 327-337, 2014.

[19] R. W. Cunningham, "Defect Formation Mechanisms in Powder-Bed Metal Additive Manufacturing," *Carnegie Mellon University,* 2018.

[20] J. V. Gordon, S. P. Narra, R. W. Cunningham, H. Liu, H. Chen, R. M. Suter, J. L. Beuth and A. D. Rollett, "Defect structure process maps for laser powder bed fusion additive manufacturing," *Additive Manufacturing,* vol. 36, p. 101552, 2020.

[21] L. Wang, Y. Zhang, H. Y. Chia and W. Yan, "Mechanism of keyhole pore formation in metal additive manufacturing," *NPJ Computational Materials,* vol. 22, 2022.

[22] J. Jakumeit, C. Huang, J. Zielinksi and J. H. Schliefenbaum, "Effect of Evaporated Gas Flow on Porosity and Microstructure of IN718 Parts Produced by LPBF-Processes," *IOP Conferences Series: Materials Science and Engineering,* vol. 861, p. 012011, 2020.

[23] I. Bitharas, N. Parab, C. Zhao, T. Sun, A. D. Rollett and A. J. Moore, "The Interplay Between Vapour, Liquid, and Solid Phases in Laser Powder Bed Fusion," *Nature Communications,* vol. 13, p. 2959, 2022.

[24] C. Qiu, C. Panwisawas, M. Ward, H. Basoalto, J. W. Brooks and M. M. Atallah, "On the role of melt flow into the surface structure and porosity development during selective laser melting," *Act Materialia,* pp. 72-79, 2015.

[25] T. Mukherjee and T. DebRoy, "Mitigation of lack of fusion defects in powder bed fusion additive manufacturing," *Journal of Manufacturing Processes,* vol. 36, pp. 442-449, 2018.

[26] P. Y. Shcheglov, A. V. Gumenyuk, I. B. Gornushkin, M. Rethmeier and V. N. Petrovskiy, "Vapor-Plasma Plume Investigation During High-Power Fiber Laser Welding," *Laser Physics,* vol. 23, p. 0166001, 2013.

[27] M. Simonelli, C. Tuck, T. N. Aboulkhair, I. Maskery, I. Ashcroft, R. D. Wildman and R. Hague, "A Study on the Laser Spatter and the Oxidation Reactions During Selective Laser Melting of 316L Stainless Steel, AL-Si10-Mg, and Ti-6Al-4V," *Metallurgical and Materials Transactions,* vol. 46, pp. 3842-3851, 2015.

[28] B. Ferrar, L. Mullen, E. Jones, R. Stamp and C. J. Sutcliffe, "Gas Flow Effects on Selective Laser Melting (SLM) manufacturing performance," *Journal of Materials Processing Technology,* vol. 212, pp. 355-364, 2012.

[29] B. Yuan, G. M. Guss, A. C. Wilson, S. P. Hau-Riege, P. J. DePond, S. McMains, M. J. Matthews and B. Giera, "Machine-Learning-Based Monitoring of Laser Powder Bed Fusion," *Advanced Materials Technologies,* vol. 3, no. 1800136, 2018.

[30] Q. Y. Lu, N. V. Nguyen, A. J. Hum, T. Tran and C. H. Wong, "Optical in-situ monitoring and correlation of density and mechanical properties of stainless steel parts produced by selective laer melting process based on varied energy density," *Journal of Materials Processing Tech.,* vol. 271, pp. 520-531, 2019.

[31] S. Feng, Z. Chen, B. Bircher, Z. Ji, L. Nyborg and S. Bigot, "Predicting laser powder bed fusion defects through in-process monitoring data and machine learning," *Materials & Design,* vol. 222, p. 111115, 2022.

[32] A. J. Dunbar, E. R. Denlinger, J. Heigel, P. Michaleris, P. Guerrier, R. Martukanitz and T. W. Simpson, "Development of experimental method for in situ distortion and temperature measurements during the laser powder bed fusion additive manufacturing process," *Additive Manufacturing,* vol. 12, pp. 25-30, 2016.

[33] O. S. Fatoba and T.-C. Jen, "Acoustic-Based In-Situ Monitoring of Additive Manufacturing Fabrication: A Review," in *International Conference on Mechanical and Intelligent Manufacturing Technologies*, Cape Town, 2023.

[34] V. Pandiyan, R. Wrobel, C. Leinenbach and S. Shevchik, "Optimizing in-situ monitoring for laser powder bed fusion process: Deciphering acoustic emission and sensor sensitivity with explainable machine learning," *Journal of Materials Processing TEch.,* vol. 321, p. 118144, 2023.

[35] J. S. Weaver, A. Schlenoff, D. C. Deisenroth and S. P. Moylan, "Inert Gas Flow Speed Measurements in Laser Powder Bed Fusion Additive Manufacturing," *NIST Advanced Manufacturing Series,* Vols. 100-43, 2021.

[36] H. Amano, Y. Yamaguchi, T. Ishimoto and T. Nakano, "Reduction of Spatter Generation Using Atmospheric Gas in Laser Powder Fusion of Ti-6Al-4V," *Materials Transactions,* vol. 62, no. 8, pp. 1225-1230, 2021.

[37] X. Li, Q. Guo, L. Chen and W. Tan, "Quantitative investigation of gas flow, powder-gas interaction, and powder behavior under different ambient pressure levels in laser powder bed fusion," *International Journal of Machine Tools & Manufacture,* vol. 170, p. 103797, 2021.

[38] S. Traore, M. Schneider, I. Koutiri, F. Coste, R. Fabbro, C. Charpentier, P. Lefebvre and P. Peyre, "Influence of gas atmosphere (Ar or He) on the laser powder bed fusion of a Ni-based alloy," *Journal of Materials Processing Technology,* vol. 288, p. 116851, 2021.

[39] H. Shen, P. Rometsch, X. Wu and A. Huang, "Influence of Gas Flow Speed on Laser Plume Attenuation and Powder Bed Particle Pickup in Laser Powder Bed Fusion," *JOM,* vol. 72, pp. 1039-1051, 2020.

[40] X.-X. Chen and W.-C. Wang, "The applications of particle image velocimetry (PIV) to experimentally observe the flow behaviors inside the Selectice Laser Melting (SLM) working chamber," *Flow Measurement and Instrumentation,* vol. 23, p. 101738, 2020.

[41] C. J. Elkins, J. Mireles, H. H. Estrada, D. W. Morgan, H. C. Taylor and R. B. Wicker, "Resolving the three-dimensional flow field within commercial metal additive manufacturing machines: Application of experimental Magnetic Resonance Velocimetry," *Additive Manufacturing,* vol. 73, p. 103651, 2023.

[42] LaVision GmbH, *Product Manual - Imager sCMOS,* Gottingen, Germany: LaVision GmbH, 2023.

[43] A. Abeyta, J. Hardy, M. Iacoviello, A. Maschhoff and Y. Pruzhanskaya, "AM Gas Flow Study Final Design Report," University of Washington, Seattle, 2023.

[44] R. Schur, *Laser Powder Bed Fusion of Ti-6Al-4V: A Round Robin Analysis of Mechanical Property Variability, Doctoral Dissertation,* Seattle: University of Washington, 2023.

[45] LaVision GmbH, "Product Manuel for Davis 10.2," Göttingen, Germany, 2022.

[46] A. Sciacchitano and B. Wieneke, "PIV uncertainty propagation," *Measurement Science and Technology,* vol. 27, p. 084006, 2016.